RELATIVE SEA-LEVEL CHANGE IN NEWFOUNDLAND, CANADA DURING THE PAST ~3000 YEARS

Andrew C. Kemp[1*], Alexander J. Wright[2], Robin J. Edwards[3], Robert L. Barnett[4,5], Matthew J. Brain[6], Robert E. Kopp[7,8], Niamh Cahill[9], Benjamin P. Horton[10,11], Dan J. Charman[5], Andrea D. Hawkes[12], Troy D. Hill[13], and Orson van de Plassche[2‡]

1. *Department of Earth and Ocean Sciences, Tufts University, Medford, MA 02155, USA*
2. *Department of Marine Biogeology, Faculty of Earth & Life Sciences, Vrije Universiteit Amsterdam, 1081 HV Amsterdam, The Netherlands*
3. *School of Natural Sciences, Trinity College Dublin, Dublin 2, Ireland*
4. *Département de Biologie, Chimie et Géographie, Université du Québec à Rimouski, Rimouski, G5L 3A1, Canada*
5. *Geography, College of Life and Environmental Sciences, University of Exeter, Exeter, EX4 4RJ, United Kingdom*
6. *Department of Geography, Durham University, Durham, DH1 3LE, United Kingdom*
7. *Department of Earth & Planetary Sciences, Rutgers University, Piscataway, NJ 08854*
8. *Institute of Earth, Ocean & Atmospheric Sciences, Rutgers University, New Brunswick, NJ 08901*
9. *School of Mathematics and Statistics, University College Dublin, Dublin 4, Ireland*
10. *Asian School of the Environment, Nanyang Technological University, Singapore*
11. *Earth Observatory of Singapore and Asian School of the Environment, Nanyang Technological University, Singapore*
12. *Department of Earth and Ocean Sciences, University of North Carolina Wilmington, Wilmington, NC 28403, USA*
13. *Louisiana Universities Marine Consortium, Chauvin, LA 70344, USA*

* *Corresponding author: andrew.kemp@tufts.edu; +1 617-627-0869*

≠ *Deceased*

Published in Quaternary Science Reviews (2018) Volume 201, pg 89-110.
https://doi.org/10.1016/j.quascirev.2018.10.012

ABSTRACT

Several processes contributing to coastal relative sea-level (RSL) change in the North Atlantic Ocean are observed and/or predicted to have distinctive spatial expressions that vary by latitude. To expand the latitudinal range of RSL records spanning the past ~3000 years and the likelihood of recognizing the characteristic fingerprints of these processes, we reconstructed RSL at two sites (Big River and Placentia) in Newfoundland from salt-marsh sediment. Bayesian transfer functions established the height of former sea level from preserved assemblages of foraminifera and testate amoebae. Age-depth models constrained by radiocarbon dates and chronohorizons estimated the timing of sediment deposition. During the past ~3000 years, RSL rose by ~3.0 m at Big River and by ~1.5 m at Placentia. A locally calibrated geotechnical model showed that post-depositional lowering through sediment compaction was minimal. To isolate and quantify contributions to RSL from global, regional linear, regional non-linear, and local-scale processes, we decomposed the new reconstructions (and those in an expanded, global database) using a spatio-temporal statistical model. The global component confirms that 20th century sea-level rise occurred at the fastest, century-scale rate in over 3000 years ($P>0.999$). Distinguishing the contributions from local and regional non-linear processes is made challenging by a sparse network of reconstructions. However, only a small contribution from local-scale processes is necessary to reconcile RSL reconstructions and modeled RSL trends. We identified three latitudinally-organized groups of sites that share coherent regional non-linear trends and indicate that dynamic redistribution of ocean mass by currents and/or winds was likely an important driver of sea-level change in the North Atlantic Ocean during the past ~3000 years.

1. INTRODUCTION

Relative sea level (RSL) varies across space and through time in response to physical processes acting on a range of spatial and temporal scales. During the ~3000 years preceding the onset of historic sea-level rise in the late 19th century, global mean sea-level change was on the order of ± 0.1 m (e.g., Kopp et al., 2016; Lambeck et al., 2014) and the primary driver of RSL change along the Atlantic coast of North America was glacio-isostatic adjustment (GIA), which varies regionally and is approximately linear over this time period (e.g., Peltier, 1996). While the magnitude and spatial pattern of global mean sea level and GIA during the past ~3000 years are relatively well understood and constrained, there remains considerable uncertainty in the contributions from regional-scale processes such as the dynamic redistribution of existing ocean mass by atmospheric and ocean circulation on timescales from years to centuries (e.g., Ezer, 2015; Levermann et al., 2005; McCarthy et al., 2015; Piecuch et al., 2016; Woodworth et al., 2017) and the changing mass and distribution of land-based ice (e.g., Mitrovica et al., 2009). These dynamic processes are non-linear during the past ~3000 years and identifying their contributions to RSL change is important for two reasons. Firstly, they will be important modulators of future global sea-level rise and therefore regional-scale RSL projections will be improved through better understanding of these processes (Church et al., 2013). Secondly, if the contribution from regional-scale processes can be isolated, then RSL reconstructions can provide insight into paleoclimate trends and events (e.g., phasing of the North Atlantic Oscillation, or strength of Atlantic Meridional Overturning Circulation) on centennial timescales that are often poorly resolved in marine sedimentary archives due to low sedimentation rates and uncertainty introduced by marine reservoir corrections applied in the calibration of radiocarbon ages (e.g., Keigwin and Boyle, 2000). However, separating regional, centennial-scale contributions to RSL

change from those caused by local processes such as sediment compaction using a sparse spatial network of RSL reconstructions is challenging.

Buried salt-marsh sediment is one of the principal sources of geological evidence for RSL changes that occurred during the past ~3000 years (e.g., Gehrels et al., 2005; Thomas and Varekamp, 1991). Salt-marsh plants and foraminifera are sea-level proxies because their vertical distribution is controlled by the frequency and duration of tidal flooding, which is correlated strongly with elevation (e.g., Edwards and Wright, 2015; Scott and Medioli, 1978). In response to RSL rise, salt-marshes accumulate sediment (including abundant plant remains that are well suited to radiocarbon dating) to maintain their position in the tidal frame and the resulting sequences of salt-marsh sediment become archives from which RSL can be reconstructed (e.g., Redfield, 1972). On the Atlantic coast of North America, the long-term RSL rise needed to create accommodation space is caused by ongoing GIA. Earth-ice models predict that the hinge line between regions experiencing GIA-driven RSL rise/fall during the past ~3000 years occurs close to the Gulf of St. Lawrence (Figure 1; e.g., Peltier, 2004). Therefore, Newfoundland is one of the most northerly regions that is likely to preserve a detailed salt-marsh record of RSL changes, which makes it an important location for investigating regional, non-linear drivers of paleo-RSL because many of these processes vary with latitude.

To expand the latitudinal range of RSL reconstructions that span the past ~3000 years along the Atlantic coast of North America, we reconstructed RSL at two sites (Big River and Placentia) in Newfoundland, Canada (Figure 1) using foraminifera and testate amoebae preserved in cores of salt-marsh sediment that we dated using radiocarbon and recognition of pollution markers of

known age. Prior to this study, similar and near-continuous RSL reconstructions were available from northeastern Florida to Nova Scotia and the Magdalen Islands (Figure 1A). We use these new reconstructions alongside published datasets to explore the role of global, regional linear, regional non-linear, and local processes as drivers of sea-level change during the past ~3000 years by decomposing RSL reconstructions using a spatio-temporal statistical model. We further quantify the role of post-depositional lowering through sediment compaction (a local-scale process) by calibrating and applying a geotechnical model to the Big River core.

2. Study Area

The number and area of salt marshes in Newfoundland is small compared to other parts of Atlantic Canada and New England (Roberts and Robertson, 1986). The sediment preserved beneath many of Newfoundland's salt marshes was described by previous research (Bell et al., 2005; Brookes et al., 1985; Daly, 2002; Daly et al., 2007; Wright and van de Plassche, 2001). Based on this body of literature and an extensive coring program in the late 1990s, we selected Big River and Placentia (~430 km apart, in western and eastern Newfoundland, respectively; Figure 1) as sites at which to develop RSL reconstructions because they had sequences of high salt-marsh peat that we anticipated (from experience and exisiting publications; e.g., Gehrels et al., 2005; Kemp et al., 2017a) would yield near-continuous and precise records of RSL change during the past ~3000 years. Reconstructing RSL at sites in western and eastern Newfoundland provides a sampling regime to better distinguish regional- and local-scale processes.

Big River is located on the Port-au-Port Peninsula, and the salt marsh occupies a small, incised valley that is protected by a beach barrier/spit at its mouth (Figure 1B–D). An adjacent salt

marsh (Hynes Brook, ~1 km away) shares a similar geomorphology. Big River and Hynes Brook have a low salt-marsh floral community of *Spartina alterniflora* (tall form) and a mixed high salt-marsh plant community comprising variable combinations of *Iris versicolor*, *Schoenoplectus* spp., *Spartina patens*, *Distichlis spicata*, *Plantago maritima*, *Triglochin maritima*, *Glyceria borealis*, *Glaux maritima*, *Agrostis stolonifera*, and *Spartina alterniflora* (short form). Although these species are frequently intermixed, some mono-specific stands are present. The great diurnal tidal range (mean lower low water, MLLW to mean higher high water, MHHW) at Big River and Hynes Brook is 1.06 m. Up to ~3 m of salt-marsh peat underlies the Big River site (Wright and van de Plassche, 2001) and previous work at Hynes Brook demonstrated that salt-marsh sediment at this depth is ~3000 years old (Bell et al., 2005; Brookes et al., 1985; Daly, 2002; Daly et al., 2007).

Placentia is located on the Avalon Peninsula (Figure 1E–F). It is indirectly connected to the ocean because the "South Arm" is closed by a gravel barrier, meaning that marine water currently reaches the site circuitously having entered through the open "North Arm". This geomorphology results in a great diurnal tidal range of 0.91 m, compared to 1.60 m at the nearby (~8 km) Argentia tide gauge that is situated on the open coast. The modern salt marsh and sequences of Holocene organic sediment lie on top of a gravel barrier system (Forbes et al., 1995). The low, gravel barrier directly in front of the salt marsh is submerged at high tide. Low salt-marsh environments are absent at the site, although isolated stands of *Spartina alterniflora* (tall form) are present and rooted in gravel rather than fine-grained sediment. The high salt-marsh is a diverse, peat-forming community that includes *Distichlis spicata*, *Spartina patens*, *Juncus geradii*, *Potentilla* sp., *Plantago maritima, Glaux maritima*, and *Carex glareosa*.

142 These plants are frequently intermixed in the high salt-marsh zone, although some mono-specific
143 stands are present. The upland edge of the salt marsh is marked by a near-vertical slope of
144 weathered bedrock that is sparsely vegetated. Daly (2002) described the sediment underlying the
145 Placentia site and noted that there was typically less than ~0.5 m of peat except in one small area
146 where up to ~1.3 m of peat was present (Figure 1H–J). Radiocarbon dates from Forbes et al.
147 (1995) and Daly et al. (2007) indicate that the bottom of this peat sequence is ~2000 years old.
148 Daly (2002) interpreted the stratigraphy at Placentia as including a unit of freshwater peat
149 between two units of salt-marsh peat. Although the possible presence of freshwater peat makes
150 the stratigraphy sub-optimal for reconstructing RSL because it would cause a temporal gap in
151 any reconstruction, we chose to work at Placentia because of the scarcity of alternative sites in
152 eastern Newfoundland and our goal of identifying regional-scale RSL trends was best met by
153 having a spatial network of reconstructions available for analysis.
154
155 **3. METHODS**
156 *3.1 Coring and sample elevations*
157 We used hand-driven cores positioned along transects to describe the sediment beneath the Big
158 River and Placentia salt marshes (Figure 1). The positioning of these transects was guided by
159 previous stratigraphic investigations of both sites (Daly et al., 2007; Wright and van de Plassche,
160 2001). A core from each site was selected for detailed analysis based on the likelihood that it
161 would produce a near-continuous reconstruction of RSL change. At Big River, core F25 was
162 chosen because it is representative of the stratigraphy at the site and included the thickest unit of
163 high salt-marsh that was not underlain by an amorphous organic unit (Figure 1G), which in our
164 experience can have a relationship to sea level that is difficult to reconstruct (e.g., Kemp et al.,

2012b). Different criteria were employed at Placentia, where we selected core C106 as being the most likely to provide a long and near-continuous reconstruction because it was located in the relatively small area of the site where the underlying topography allowed a relatively thick sequence of sediment to accumulate (Figure 1H–J) and also did not (at least visibly) include the unit of amorphous (potentially freshwater) organic material. Therefore, C106 is representative of only of a small part of the stratigraphic record at Placentia. We recovered each core in overlapping, 50-cm long sections using an Eijelkamp Russian-type peat sampler. Each section was placed in a rigid plastic sleeve, wrapped in plastic, and kept refrigerated until processing in the laboratory to minimize desiccation and/or decay.

Core-top elevations were measured in the field by leveling each core site to a temporary benchmark using a total station. The tidal elevation of the temporary benchmarks was previously established by deploying water-level loggers at each site and comparing local tides to those at nearby tide gauge stations (Kemp et al., 2017c; Wright et al., 2011). We analyzed observed water levels from 1st January 1983 to 31st December 2001 from the Port-aux-Basques and Argentia tide gauges (Figure 1) and extracted high and low tides using the "*Tides*" package (Cox, 2016) for R (R Development Core Team, 2017). The water-level data was downloaded from the Canadian Hydrographic Service (Argentia: http://www.isdm-gdsi.gc.ca/isdm-gdsi/twl-mne/inventory-inventaire/sd-ds-eng.asp?no=835&user=isdm-gdsi&region=ATL&ref=maps-cartes. Port-Aux-Basques: http://www.isdm-gdsi.gc.ca/isdm-gdsi/twl-mne/inventory-inventaire/sd-ds-eng.asp?no=665&user=isdm-gdsi&region=ATL&ref=maps-cartes). From this observation period, we calculated tidal datums following the definitions used by the National Oceanic and Atmospheric Administration (NOAA) for the 1983–2001 tidal epoch.

188

189 *3.2 Dating*

190 The cores from Big River and Placentia were dissected to isolate individual plant macrofossils
191 found in growth position. Each macrofossil was identified through comparison with modern
192 specimens collected in the field and published descriptions (e.g., Niering et al., 1977). From this
193 suite of samples, we selected macrofossils for radiocarbon dating based on size, preservation
194 state, and their distribution throughout each core. The selected samples were cleaned under a
195 microscope to remove adhered sediment and ingrowing rootlets, after which they were dried at
196 ~40 °C and submitted for dating. Samples from Big River were dated at the Utrecht van der
197 Graaf Laboratorium and samples from Placentia were dated at the National Ocean Sciences
198 Accelerator Mass Spectrometry (NOSAMS) facility. At both laboratories, each sample
199 underwent acid-base-acid pre-treatment and conversion to a graphite target. $\delta^{13}C$ was measured
200 on an aliquot of CO_2 collected during sample combustion. Radiocarbon results (Table 1) from
201 Utrecht were originally reported without rounding, while those from NOSAMS were rounded
202 following Stuiver and Polach (1977). To ensure comparability among sites, we rounded the
203 reported radiocarbon ages and their uncertainties from the Utrecht laboratory prior to any further
204 analysis following the conventions of Stuiver and Polach (1977). Three samples in the Placentia
205 core were dated more than once as part of a quality control procedure at NOSAMS (Table 1). At
206 each depth the replicate measurements were performed on the same individual plant macrofossil
207 (as opposed to multiple samples from the same depth) and we therefore created a pooled mean
208 for these depths using the Calib software (Stuiver et al., 2017) prior to any further analysis.

209

Due to a plateau in the calibration curve, radiocarbon dates on material younger than ~1600 CE often return multiple possible ages and large uncertainty. To develop a chronology with the desired precision for the past ~400 years, we recognized pollution horizons of known age in downcore profiles of elemental and isotopic abundance. ^{137}Cs activity was measured by gamma counting at Yale University using the methods and instrument described in Hill and Anisfeld (2015). We used 1-cm thick samples spaced at 2-cm intervals in the topmost parts of the Big River and Placentia cores to measure elemental abundance and lead-isotope ratios using mass spectrometry. The samples were oven dried at 40 °C and ground to a fine, homogenized powder that was analyzed by inductively coupled plasma mass spectrometry at a commercial laboratory (SGS Mineral Services).

We generated an age-depth model for each core using Bchron (Haslett and Parnell, 2008; Parnell et al., 2008). Since we obtained radiocarbon dates on rhizomes of salt-marsh plants, an uncertainty and depth correction was added to the Bchron input to reflect that these macrofossils likely grew at 2 cm ± 2 cm below the paleo marsh surface that we sought to date. Radiocarbon dates were calibrated individually by Bchron using the IntCal13 calibration curve (Reimer et al., 2013). Marker horizons identified in downcore profiles of elemental abundance, isotopic activity, and isotopic ratios were assumed to have a normally-distributed temporal uncertainty. We also assigned a thickness uncertainty to each horizon to reflect that the chronological marker could occur in more than one sample. From this input Bchron generated a large suite of equally-probable accumulation histories that were summarized by a probability density function to estimate the age of every 1-cm thick sample in the core with uncertainty. Throughout the text, chronological uncertainties from Bchron age-depth models are reported as the 95% credible

233 interval. We also used Bchron to estimate annual sediment accumulation with uncertainty
234 (reported as the 90% credible interval; 5^{th}–95^{th} percentiles).
235
236 *3.3 Foraminifera and Testate Amoebae*
237 Every other 1-cm thick sample from each core was prepared for foraminiferal analysis by sieving
238 the sediment under running water to retain the 63–500 μm fraction, from which we counted a
239 minimum of 100 foraminifera. If fewer than 100 tests were present, then the entire sample was
240 counted. Taxonomy followed Wright et al. (2011) and Kemp et al. (2017c); most notably, counts
241 of *Jadammina macrescens* and *Balticammina pesudomacrescens* were combined. Since these
242 species often co-exist and have similar relationships to tidal elevation this decision is unlikely to
243 affect the resulting RSL reconstruction, but does minimize the likelihood of bias being
244 introduced by taxonomic inconsistencies among workers.
245
246 Following preliminary analysis of the Placentia core, we identified an interval (~60–16 cm;
247 1330–1870 CE) with few or no foraminifera due to their absence or poor preservation. To avoid
248 a gap in the RSL reconstruction from Placentia, we analyzed testate amoebae from this interval
249 following Barnett et al. (2013; after Charman et al., 2000). A subsample of 1 cm^3 sediment was
250 combined with a *Lycopodium clavatum L*. tablet (to calculate concentration; Stockmarr, 1971) in
251 100 ml of deionized water and heated at 80 °C for one hour to aid disaggregation. The solution
252 soaked for ~12 hours prior to wet sieving to retain the 15–300 μm fraction. Retained sediment
253 was mounted on glass slides with a water-glycerol solution for counting. We aimed to count 100
254 tests per sample, but where test-concentration was low (<2000 tests/cm^3), a minimum of 60 tests

were counted (e.g., Charman et al., 2010). Identifications followed the taxonomy of Barnett et al. (2017b), which was developed for intertidal salt-marsh testate amoebae of the North Atlantic.

3.4 Compaction

Salt-marsh sediments are prone to compaction (physical compression and biodegradation) that can cause post-depositional lowering of samples used to reconstruct RSL (Bloom, 1964; Brain, 2016; Long et al., 2006). Post-depositional lowering results in an overestimation of the magnitude and rate of reconstructed RSL rise (e.g., Shennan and Horton, 2002). We estimated post-depositional lowering of samples in the Big River core using the geotechnical modelling approach of Brain et al. (2011, 2012, 2015). Post-depositional lowering was not estimated for the Placentia core because it is considerably shorter (and therefore less prone to compaction through physical compression) than the Big River core. As such, Big River likely represents an upper limit for the contribution from compaction to RSL reconstructions derived from unbroken sequences of high salt-marsh sediment in Newfoundland. To provide the empirical data that are necessary to calibrate the geotechnical model, we collected 11 undisturbed surface sediment samples from Big River, Hynes Brook, and Placentia, ensuring that samples were obtained from the range of eco-sedimentary zones encountered (Figure 1; Table 2). For each sample we measured (1) organic content by loss-on-ignition (LOI; three determinations per sample); (2) specific gravity (G_s) using gas pycnometry (one determination per sample; Head, 2008); and (3) compression behaviour using automated oedometer testing (Head and Epps, 2011; Rees, 2014). From these measurements we established empirical relationships between LOI and specific gravity, and between LOI and the compression properties of modern salt-marsh sediments. For contiguous, 2-cm thick samples in the Big River core, we measured LOI and dry bulk density

and then used the empirical relationships established from modern, analogous sediments to estimate the compression properties of each sample. In each modelled layer in each model run, we assigned values of the compressive yield stress, σ'_y, by sampling from a continuous, triangular probability distribution, defined by the modal value and range of σ'_y observed in surface sediment (Table 2). We applied the geotechnical model using a Monte Carlo approach (5000 runs) to estimate depth-specific post-depositional lowering with uncertainty (± 1 standard deviation). To assess the predictive capacity of the model, we compared measured and model-derived estimates of dry bulk density.

3.5 Reconstructing relative sea level

We reconstructed paleomarsh elevation (the tidal elevation at which a sample originally accumulated) using two independent Bayesian transfer functions. The foraminifera-based transfer function was calibrated using an empirical modern training set of 134 surface sediment samples collected along intertidal transects at Big River, Hynes Brook, and Placentia (Kemp et al., 2017c; Wright et al., 2011; Figure 1). Sample elevations were expressed as a standardized water level index because great diurnal tidal range varied among sites. Throughout the manuscript we use F-SWLI in reference to the standardized water level index used for foraminifera. A value of 100 equates to local mean tide level and a value of 200 is the highest occurrence of foraminifera at each site. Wright et al. (2011) proposed that using the highest occurrence of foraminifera as a datum resulted in more reliable paleomarsh elevation reconstructions than using a tidal datum such as MHHW. Foraminiferal abundance was expressed as raw counts and core samples that yielded fewer than 50 foraminifera were excluded from the final RSL reconstruction.

The testate amoebae transfer function was calibrated on the North Atlantic dataset described in Barnett et al. (2017b) with additional data from Big River, Hynes Brook, and Placentia (Kemp et al., 2017c). The resulting dataset comprised 308 samples from 17 sites. Sample elevations were expressed as a standardized water level index, where zero is the lowest occurrence of testate amoebae and 100 is highest astronomical tide. Throughout the manuscript, we use T-SWLI in reference to the standardized water level index used for testate amoebae. The training set of testate amoebae was modified by condensing and reducing the number of taxa in the dataset to improve the Bayesian transfer function performance and to reduce computation time (which also depends on the number of samples). In the BTF it is more difficult to achieve convergence of model parameters if there are many rare species and/or if the number of species approaches the number of samples available compared to when there are few rare taxa and considerably more samples than species. Furthermore, computation time is reduced by analyzing fewer taxa, although even with all taxa the analysis is completed on a timescale of hours (for example, building the BTF for foraminifera took ~27 hours of computational time). Taxa and groups of taxa with invariant ecological tolerance ranges (established by weighted averaging regression of the species data) were combined to reduce the number of taxa and groups from 53 to 38 without reducing the number of samples in the modern dataset. Low occurrence taxa were removed following Legendre and Birks (2012). Taxa occurring in only one sample (then 2, 3,…*n* samples…) were removed from the dataset until taxa variation (canonical correspondence analysis axis 1 eigenvalue as a percentage of total inertia) explained by changes in elevation became negatively affected by the removal. This resulted in the removal of 16 low-occurring

taxa/groups that were encountered in 15 or fewer samples, with no loss in the amount of species variation explained by elevation.

The two Bayesian transfer functions were developed following the approach described in Cahill et al. (2016). This approach assumes a multinomial model for foraminiferal/testate amoebae assemblages, and uses a set of penalized spline smoothing functions (Lang and Brezger, 2004) to describe the non-linear relationship between each taxa and tidal elevation. The parameters that describe each taxon response curve were estimated empirically from the modern training set. Performance of the Bayesian transfer functions was measured by 10-fold cross validation. When applied to fossil assemblages of foraminifera/testate amoebae preserved in the Big River and Placentia cores, the BTFs returned a paleomarsh elevation reconstruction (in F-SWLI/T-SWLI units) with a sample-specific 95% uncertainty interval. Paleomarsh elevations were converted to absolute tidal elevations using the modern relationship between local tidal datums at each site. This approach therefore assumes a constant tidal range through time.

RSL was reconstructed by subtracting paleomarsh elevation estimated by the Bayesian transfer functions from sample elevation, where both values are expressed relative to the same tidal datum. Sample elevation was measured as depth in core, where the core-top elevation was measured in the field (as described in Kemp et al., 2017c) and this term is considered to be a fixed and known value. The corresponding age of each sample (with uncertainty) was provided by the Bchron age-depth model.

If an assemblage of foraminifera and/or testate amoebae preserved in core sediment lacks an appropriate modern analog, then the reconstructed paleomarsh elevation may not be ecologically plausible (e.g., Jackson and Williams, 2004; Simpson, 2012). To quantify the degree of analogy, we measured dissimilarity between each core sample and its closest analog in the modern training set using the Bray-Curtis metric. If this value exceeded the 20th percentile of dissimilarity measured in all possible pairings of modern samples, then we determined that the core sampled lacked a modern analog and it was excluded from the final RSL reconstruction. The choice of the 20th percentile as a threshold for dissimilarity is common for populations such as foraminifera that form low-diversity assemblages, particularly in instances where the distribution of modern samples is uneven (i.e. concentration at particular elevations such as mean tide level to MHHW for foraminifera; Figure 2) since this causes dissimilarity measured among pairs of modern samples to be biased low (e.g., Kemp and Telford, 2015). For higher diversity populations, it may be appropriate to use a lower percentile of dissimilarity in determining the threshold for whether or not a core sample has a modern analog (Jackson and Williams, 2004; Watcham et al., 2013).

3.6 Statistical analysis of relative sea-level reconstructions

To self-consistently estimate (with uncertainty) differences in RSL among locations, rates of RSL change, and to distinguish among the global, regional linear, regional non-linear, and local components of RSL change, we employed a spatio-temporal empirical hierarchical model (e.g., Kopp et al., 2016) . The input data for the model are the global database of RSL reconstructions in Kopp et al. (2016) after it was updated to include the Big River and Placentia reconstructions (this study; uncorrected for post-depositional lowering) and recently-published records (Figure

1A) from North Carolina (Kemp et al., 2017b), New York City (Kemp et al., 2017a), the Gulf Coast of Florida (Gerlach et al., 2017), and the Magdalen Islands (Barnett et al., 2017a). Tide-gauge records were updated from the Permanent Service for Mean Sea Level (Holgate et al., 2013) to include data through 2017. As in Kopp et al. (2016), the input data also include the global mean sea-level reconstruction of Hay et al. (2015), that was generated from tide-gauge records. Posterior estimates generated by the spatio-temporal model for sites in eastern North America are provided in the supporting information.

The model has (1) a process level that characterizes the behavior of RSL over space and time, (2) a data level that links RSL observations (reconstructions) to the RSL process, and (3) a hyperparameter level that characterizes prior expectations regarding dominant spatial and temporal scales of RSL variability.

At the process level, we model the RSL field $f(\mathbf{x},t)$ as the sum of seven components:

$$f(\mathbf{x},t) = g_f(t) + g_s(t) + m(\mathbf{x})(t - t_0) + r_s(\mathbf{x},t) + r_f(\mathbf{x},t) + l_s(\mathbf{x},t) + l_f(\mathbf{x},t) \quad (1)$$

where $\mathbf{x}$ represents geographic location, t represents time, and t_0 is a reference time point (2000 CE). The seven components are: fast and slow common (global) terms, $g_f(t)$ and $g_s(t)$, representing the time-variable signal shared by all sites that are included in the analysis; a regionally varying, temporally linear (on the timescale under examination) term, $m(\mathbf{x})(t\text{-}t_0)$, which represents slowly changing processes such as GIA and/or tectonics (Engelhart et al., 2009); regionally varying, fast and slow temporally non-linear fields, $r_f(\mathbf{x},t)$ and $r_s(\mathbf{x},t)$, which primarily represent factors such as dynamic sea level and the fingerprints of land-ice melt, and fast and slow local fields, $l_f(\mathbf{x},t)$ and $l_s(\mathbf{x},t)$, which represent site-specific processes such as

391 sediment compaction. As in Kopp et al. (2016), the common global signal is assumed to average
392 0 mm/yr over 0–1700 CE.
393
394 The data level of the spatio-temporal model represents the inherently noisy RSL reconstructions
395 (comprised of multiple data points termed observations; y_i) as:
396 $$y_i = f(\mathbf{x}_i,t_i) + \varepsilon_i + w(\mathbf{x}_i,t_i) + y_0(x_i) \quad (2)$$
397 $$t_i = \hat{t}_i + \delta_i \quad (3)$$
398 where $f(\mathbf{x}_i,t_i)$ is the true RSL value at location $\mathbf{x}$ and time t; ε_i is the vertical uncertainty of the
399 RSL observation i; $w(\mathbf{x}_i,t_i)$ is supplemental white noise added to capture incompleteness of the
400 process model and under-estimation of vertical and temporal measurement error; and $y_0(\mathbf{x}_i)$ is a
401 site-specific vertical datum correction that is applied to ensure that the independent RSL
402 reconstructions are directly comparable to one another. The true age of a RSL observation (t_i)
403 includes the mean estimate of the true age ($\hat{t}_i$) and its chronological error (δ_i), which is
404 approximated using the noisy-input Gaussian process method (McHutchon and Rasmussen,
405 2011).
406
407 The priors for each term in the model are Gaussian processes (Rasmussen and Williams, 2005)
408 with Matérn covariance functions (see Kopp et al., 2016 for more details). All priors have zero
409 mean except for the regional-scale linear component, $m(\mathbf{x})$, which uses predictions from the
410 ICE5G–VM2–90 Earth-ice model (Peltier, 2004) as prior means. This does not significantly
411 affect the final (posterior) estimate of the regional-scale linear component, which the model
412 estimates based on the observations. Hyperparameters defining prior expectations for the
413 amplitudes and spatio-temporal scales of variability were set through a maximum-likelihood

optimization. The non-linear terms were characterized by three spatial scales (global, regional, and local) and two temporal scales (fast and slow; Table 3). These different spatial and temporal scales enable RSL to be decomposed and can be thought of as akin to filters of different spatial and temporal bandwidths. Optimized values indicate that the dominant temporal scales are 326 years for the slow terms and 12 years for the fast terms, the dominant regional spatial scale is 6.1° angular distance, and the local spatial scale is 0.05°. The largest non-linear signal comes from the slow, global term (prior standard deviation of 16 cm), followed by the slow, regional term (prior standard deviation of 6 cm). The fast, regional term and the two local terms make comparable contributions (prior standard deviations of 2–3 cm). The supplemental white noise and datum correction terms are negligible, which indicates that the stated measurement errors are adequate to explain the differences between the process model and the observations.

4. RESULTS

4.1 Performance of Bayesian transfer functions

The Bayesian transfer function developed for foraminifera utilized a modern training set (134 samples from three sites in Newfoundland) that spanned an elevational range of 84–200 F-SWLI. Under 10-fold cross validation there is a strong (r^2=0.81) relationship between actual (measured at the time of sample collection) and predicted elevation (Figure 2). Within their uncertainty, the predicted elevation of 96% (128 of 134) of samples included the actual elevation. Absolute residuals (difference between actual and predicted elevation) averaged 3.3 F-SWLI, with a standard deviation of 3.2 F-SWLI, and a maximum of 46.8 F-SWLI. The lack of any systematic relationship between residuals and actual elevation (r^2=0.05) indicates that the foraminiferal Bayesian transfer function should produce unbiased reconstructions of paleomarsh elevation.

437

438 The Bayesian transfer function developed for testate amoebae utilized a modern training set (308
439 samples from sites in the North Atlantic Ocean, including three sites in Newfoundland) that
440 spanned an elevational range of 0–435 T-SWLI. Under 10-fold cross validation there is a strong
441 (r^2=0.67) relationship between actual and predicted elevation (Figure 2). Within their
442 uncertainty, the predicted elevation of 80% (247 of 308) of samples included the actual
443 elevation. Of the 61 samples for which the Bayesian transfer function did not accurately predict
444 elevation, a disproportionate number came from Sillons (14 samples) in the Magdelen Islands
445 (Canada) and Scheldt Estuary (16 samples) in Belgium, which may indicate local-scale
446 variability in the distribution of testate amoebae. Absolute residuals averaged 33 T-SWLI, with a
447 standard deviation of 29 T-SWLI, and a maximum of 157 T-SWLI. The lack of any systematic
448 relationship between residuals and actual elevation (r^2=0.001) indicates that the testate amoebae
449 Bayesian transfer function should produce unbiased reconstructions of paleomarsh elevation.

450

451 *4.2 Relative sea level at Big River*

452 The stratigraphy beneath Big River is comprised primarily of high salt-marsh peat with abundant
453 plant remains overlying an incompressible substrate of consolidated, grey-blue silt and clay of
454 glacial origin (Figure 1G). Within the high salt-marsh peat are thin (< 5 cm) and discontinuous
455 horizons containing increased fine-grained clastic sediment. The discontinuous nature of these
456 units likely indicates that they are the result of a process operating intermittently and on
457 meter-scales, such as delivery of ice-rafted sediment (Richard, 1978). Pools (diameters on the
458 order of a few meters and lifespans of years) are also a common feature of salt marshes in the

study region and are associated with deposition of fine-grained minerogenic sediment that could leave thin clastic layers in the sedimentary record (e.g., Wilson et al., 2014; Wilson et al., 2010). A total of 42 radiocarbon ages obtained on plant macrofossils in core F25 (Table 1; Figure 3) reveal that the uppermost 3.05 m of sediment accumulated during the past ~3000 years.

We assigned the lowest depth in the Big River core with detectable ^{137}Cs activity (21 ± 2 cm) an age of 1954 CE ± 2 years and the depth with maximum activity (13 ± 2 cm) was recognized as 1963 CE ± 1 year (Figure 3A). These horizons represent the initiation and peak of above-ground testing of nuclear weapons respectively (see discussion in Wright et al., 1999 for example). Prevailing westerly winds carried pollution from the major industrial centers in the United States (including the Upper Mississippi Valley and northeastern states) to Newfoundland and we therefore used historic emissions from the United States to assign ages to downcore trends in elemental and isotopic abundance (Figure 3A). Our interpretation relies on trends rather than absolute values since emissions per unit of production likely changed through time. We assume that pollution was deposited principally onto the high salt-marsh surface from the atmosphere, shortly after emission and without further isotopic fractionation. The ratio of lead isotopes (^{206}Pb:^{207}Pb) measured in bulk core sediment reflects the evolving sources of lead pollution that began in North America with processing of galena ore with a distinctive isotopic signature in the Upper Mississippi Valley (Doe and Delevaux, 1972; Heyl et al., 1966; Kemp et al., 2012a; Lima et al., 2005). The initial increase in ^{206}Pb:^{207}Pb (35 ± 2 cm) is interpreted as reflecting the start of emissions from the Upper Mississippi Valley and correspondingly assigned an age of 1827 CE ± 5 years. A peak in ^{206}Pb:^{207}Pb (29 ± 2 cm) occurred in 1858 ± 5 years when the quantity of lead produced in the Upper Mississippi Valley reached its maximum proportion of U.S. national

output. The decline of lead production in the Upper Mississippi Valley coupled with growing production elsewhere from sources with less distinctive isotopic ratios caused ^{206}Pb:^{207}Pb to reach a minimum in 1880 CE ± 20 years (25 ± 2 cm). The onset of widespread industrialization at 1875 CE ± 5 years caused a corresponding increase in the quantity of lead deposited at Big River (25 ± 2 cm), while the introduction of the Clean Air Act reduced lead pollution (1974 CE ± 5 years) at Big River (13 ± 2 cm). We attribute the second rise in lead (at depths above 13 cm in the Big River core) to local trends of unknown provenance since similar features are not observed elsewhere in the northeastern United States or eastern Canada (e.g., Chillrud et al., 1999; Gobeil et al., 2013; Graney et al., 1995; Kemp et al., 2015). Assimilation of the radiocarbon dates and pollution markers into a Bchron age-depth model allowed us to reconstruct the history of sediment accumulation at Big River (Figure 3B). The chronological uncertainty for a 1-cm thick sample in this core (measured by the mean width of the 95% credible interval) was ± 53 years. Prior to ~1850 CE the mean annual rate of sediment accumulation was 0.65 mm/yr (95% credible interval of 0.20–2.8 mm/yr), after which the rate increased to 0.9 mm/yr (95% credible interval of 0.28–3.8 mm/yr), including a current rate of ~2.0 mm/yr (95% credible interval of 0.6–10.0 mm/yr; Figure 3C).

Foraminifera were counted in 151, 1-cm thick samples from the Big River core. In these samples, *Jadammina macrescens*/*Balticammina pseudomacrescens* was the single most abundant taxon at most depths (60% of all counted individuals; Figure 4). Foraminifera were present at depths below 288 cm, but these samples yielded fewer than 50 individual tests (almost exclusively *Jadammina macrescens*/*Balticammina pseudomacrescens*). From 288 cm to 222 cm, there was elevated relative abundance of *Miliammina fusca* (average 38%). Similarly, the

505 intervals at depths of 178–164 cm and 126–124 cm were characterized by assemblages that
506 included more than 25% *Miliammina fusca*. At 138–38 cm assemblages of foraminifera included
507 an average of 20% *Haplophragmoides* spp. *Tiphotrocha comprimata* was present throughout the
508 core, but most abundant (average 27%) above 56 cm. Only one sample (at 40 cm) lacked an
509 appropriate analog in the modern training set (at the 20th percentile of dissimilarity) and two
510 samples above 288 cm contained fewer than 50 foraminifera (Figure 4). These samples (along
511 with the seven samples below 288 cm with low counts) were excluded from the final RSL
512 reconstruction. When the threshold for dissimilarity was lowered to the 10th/5th percentile, the
513 number of foraminiferal assemblages lacking a modern analogue was 10/85 out of a total of 151
514 samples. Application of the Bayesian transfer function to assemblages of foraminifera preserved
515 in the Big River core generated paleomarsh elevation reconstructions with sample-specific
516 uncertainties. For samples with <20% *Miliammina fusca*, the average reconstructed paleomarsh
517 elevation was 162 F-SWLI. In comparison, samples with >20% *Miliammina fusca* produced
518 paleomarsh elevation reconstructions with an average of 133 F-SWLI. The average uncertainty
519 in paleomarsh elevation reconstructions (95% credible interval) was ± 25 F-SWLI, which is ±
520 0.23 m under our assumption of a stationary tidal regime at Big River.

521

522 At Big River, RSL rose continuously from approximately –2.64 m at –800 CE (Figure 5). The
523 rate of RSL rise estimated by the spatio-temporal model was 0.60 ± 0.15 mm/yr (95% credible
524 interval) until 0 CE. Over the period 0–1700 CE, RSL rose at 0.98 ± 0.05 (95% credible interval)
525 and during the 20th century the rate of rise was 2.05 ± 0.61 mm/yr (95 credible interval). In
526 comparison, the tide gauge at Port-aux-Basques recorded a linear rate of rise of ~2.2 mm/yr over
527 the period 1959–1999 CE. Therefore, within uncertainty the tide gauge and RSL reconstruction

528 record the same rate of historic rise. The data used to reconstruct RSL at Big River are tabulated
529 in the supporting information.

530

531 *4.3 Relative sea level at Placentia*

532 The stratigraphy underlying the Placentia site is comprised of up to ~1.75 m of organic sediment
533 overlying basal sand (Figure 1 H–J). A unit of red-hued, highest salt-marsh peat lies above the
534 basal sand. At most coring locations, this unit was replaced upcore by an amorphous, black
535 organic unit that outcrops at the surface in a few locations and which Daly (2002) interpreted as
536 a detrital, freshwater peat. A unit of brown-coloured, high salt-marsh peat is present at most
537 locations on the marsh surface. We selected core C106 for detailed analysis because it included
538 the thickest highest salt-marsh unit and the freshwater peat appeared to be absent. Visual
539 inspection of cores in the field and of C106 in the laboratory did not reveal any clear evidence
540 for a hiatus or disturbance events. Radiocarbon dates from 19 depths in the core (including three
541 depths where pooled means were generated from replicate radiocarbon measurements; Table 1)
542 reveal that this sediment accumulated during the past ~2750 years (Figure 6B). Our
543 interpretation of isotopic and elemental profiles in the upper ~0.3 m of the core followed our
544 interpretation of similar measurements on the Big River core (Figure 3A). In addition to the
545 chronological horizons recognized at Big River, we identified the onset of copper pollution
546 (1900 CE ± 10 years) at 13 ± 4 cm in the Placentia core (Figure 6A), alongside a peak in lead
547 deposition following World War One (1925 CE ± 5 years at 11 ± 4 cm), a reduction in lead
548 deposition during the Great Depression (1935 CE ± 6 years at 9 ± 6 cm), a minimum in the
549 ^{206}Pb:^{207}Pb ratio caused by the changing source of lead being added to vehicle fuel (1965 CE ± 5
550 years at 8 ± 2 cm) and a peak in vanadium concentration (1974 ± 5 years at 5 ± 4 cm) that we

551 interpreted as confirmation that peak pollution was curtailed by the introduction of the Clean Air
552 Act in the United States. Assimilation of these dates using Bchron, generated an age-depth model
553 with an average uncertainty (95% credible interval) of ± 75 years for 1-cm thick samples,
554 although we note that below depths of 137 cm, the uncertainty is greater (Figure 6B). The history
555 of sedimentation at Placentia includes distinctive pulses of sedimentation and a prolonged period
556 of no/slow deposition (Figure 6C). Faster sedimentation occurred at approximately –500 CE to –
557 250 CE (average 0.58 mm/yr; 0.17–2.4 mm/yr, 95% credible interval) and at ~1300 CE to ~1500
558 CE (average 0.94 mm/yr; 0.24–4.2 mm/yr, 95% credible interval), when the mean annual rate
559 reached a maximum of 3.3 mm/yr. From 100 CE to 1000 CE the average mean annual rate of
560 sedimentation was positive, but slow (average 0.11 mm/yr; 0.03–0.39 mm/yr, 95% credible
561 interval).

562

563 Assemblages of foraminifera in the Placentia core were characterized at all depths by high
564 abundances of *Jadammina macrescens*/*Balticammina pseudomacrescens* (minimum of 81% in
565 all samples that yielded representative counts below 4 cm), although in the uppermost 4 cm,
566 *Trochammina inflata* comprised ~50% of the assemblage (Figure 7). Foraminifera were scarce
567 (1–16 tests in 1-cm thick samples), or absent from 60 cm to 16 cm. Application of the Bayesian
568 transfer function to these assemblages indicates that the sediment above 16 cm and below 60 cm
569 was deposited in the uppermost part of the intertidal zone close to highest astronomical tide and
570 the highest occurrence of foraminifera. The average (95% credible interval) uncertainty for
571 reconstructed paleomarsh elevation was ± 15 F-SWLI (equivalent to ± 0.12 m at Placentia). All
572 assemblages of foraminifera in the core had analogues in the modern training set when the 20th
573 percentile of dissimilarity was employed as a threshold. When the threshold was lowered to the

574 $10^{th}/5^{th}$ percentile, the number of foraminiferal assemblages lacking a modern analogue was 0/6
575 out of a total of 61.

576

577 The top 60 cm of the Placentia core was analysed for testate amoebae because of the scarcity or
578 absence of foraminifera (Figure 7). Testate amoebae assemblages were typical of salt-marsh
579 environments around the North Atlantic Ocean, including Newfoundland (Figure 7). From ~60
580 cm to ~20 cm the most common taxa were *Centropyxis aculeata* type (15–39%), *Centropyxis*
581 *cassis* type (14–47%), and *Tracheleuglypha dentata* type (up to 17%). Above ~20 cm, the
582 abundance of *Pseudocorythion* type increased (up to 68%), while there was a corresponding
583 reduction in the abundance of *Centropyxis aculeata* type (less than 38%) and *Centropyxis cassis*
584 type (less than 36%). Application of the Bayesian transfer function to these assemblages
585 generated paleomarsh elevation reconstructions that indicate deposition in a high salt-marsh
586 environment below highest astronomical tide (and notably below the highest occurrence of
587 foraminifera in the modern training set; Figure 7). The average uncertainty (95% credible
588 interval) for the paleomarsh elevation reconstructions was ± 65 T-SWLI (equivalent to ± 0.28 m
589 at Placentia), although we note that two samples (at 28 cm and 24 cm) had particularly large
590 uncertainties of ± 172 T-SWLI and ± 177 T-SWLI respectively. All assemblages of testate
591 amoebae had an analogue in the modern training set from the North Atlantic Ocean when the
592 20^{th} percentile was used as a cut-off value. Using the $10^{th}/5^{th}$ percentile instead, resulted in 1/20
593 samples lacking a modern analogue.

594

595 At Placentia, paleomarsh elevation exhibited little variability until ~1970 CE (~6 cm depth;
596 Figure 7). Therefore, reconstructed RSL trends prior to ~1970 CE arise primarily from changes
597 in the rate of sediment accumulation. The reconstructed mean annual sedimentation rate (Figure
598 6C) only exceeded 1 mm/yr in 137 years out of a total record length of more than 2500 years
599 (mean annual sedimentation exceeding 2/3/4 mm/yr occurred in 18/5/0 years). These rates of
600 accumulation and the corresponding rates of time-averaged RSL rise are well below proposed
601 upper limits of salt-marsh sedimentation (e.g, Kirwan et al., 2010; Kirwan et al., 2016; Morris et
602 al., 2002), indicating that the consistency of reconstructed paleomarsh elevation is ecologically
603 plausible. Importantly, the switch to using testate amoebae as sea-level indicators in the absence
604 of foraminifera did not cause a marked change in paleomarsh elevation (Figure 7). Foraminifera
605 below 60 cm indicated that paleomarsh elevation was above local MHHW and below highest
606 astronomical tide, while testate amoebae from 60 cm to ~16 cm also show paleomarsh elevation
607 in this range.

608

609 Placentia offers an opportunity to consider similarities and differences between
610 paleoenvironmental inferences drawn from foraminifera and testate amoebae. At depths of 16–60
611 cm, 13 samples contained no foraminifera and 10 yielded 1–16 tests. We consider three possible
612 explanations for the absence/scarcity of foraminifera in this interval. Firstly, the rate of sediment
613 accumulation was sufficiently high to dilute the concentration of foraminifera and produce low
614 counts. This seems unlikely, particularly in light of age-depth results, which indicate that the rate
615 of sediment accumulation was not unusual for a salt-marsh experiencing RSL rise (Figure 6C).
616 Other studies, show that foraminifera are abundant in salt-marsh sediment accumulating at these
617 rates (e.g., Kemp et al., 2013). Secondly, this section of core was deposited at, or above, the

618 highest occurrence of foraminifera and therefore no or few tests were ever present. The
619 absence/scarcity of foraminifera does coincide with faster sediment accumulation (Figure 6) that
620 was sufficiently high perhaps to cause emergence. However, results from the testate amoebae
621 transfer function (Figure 7) indicate that the sediment accumulated close to MHHW, in which
622 case it is reasonable to assume that a healthy population of agglutinated foraminifera existed on
623 the paleo salt-marsh surfaces if the paleoenvironmental interpretation of testate amoebae is
624 accurate. Furthermore, core stratigraphy does not indicate a change in depositional environment.
625 Cross validation of the testate amoebae Bayesian transfer function (Figure 2) does not indicate
626 that is likely to generate systematically biased paleomarsh elevation reconstructions. Thirdly,
627 foraminifera were present on the paleomarsh surfaces, but poorly preserved (hence only a
628 handful of tests being found in core samples). Other studies (e.g., Kemp et al., 2014; Kemp et al.,
629 2013) also noted the absence/scarcity of foraminifera in sections of cores where supporting
630 evidence such as plant macrofossils or bulk-sediment geochemistry strongly suggest deposition
631 in a high-salt marsh environment that probably supported agglutinated foraminifera. In the upper
632 6 cm of the Placentia core, testate amoebae recorded an increase in paleomarsh elevation
633 (emergence), while an increase in *Trochammina inflata* drove a modest decrease in paleomarsh
634 elevation (drowning) estimated using foraminifera. Although these trends are contradictory, they
635 are not significant within the reconstruction uncertainties.

636

637 At Placentia, RSL rose continuously from –1.40 m at –760 CE. The rate of RSL rise estimated
638 by the spatio-temporal model was 0.48 ± 0.06 (95% credible interval) over the period 0–1700
639 CE, but during this interval the rate of RSL included phases of slower (0.12 ± 0.27 for 400–800
640 CE; 95% credible interval) and faster rise (1.07 ± 0.23 for 1200–1600 CE; 95% credible

641 interval). During the 20th century the rate of rise was 1.43 ± 0.62 mm/yr (95% credible interval).
642 For comparison, the Argentia tide gauge measured a linear rate of RSL rise of 1.33 mm/yr
643 between 1971 CE (first year of measurements) to 2000 CE. Therefore, within uncertainty the tide
644 gauge and RSL reconstruction record the same rate of historic rise (albeit over a limited time
645 interval). It is important to recognize that the short duration (29 years) of this instrumental record
646 may not be suitable for accurately representing sustained RSL trends because of contamination
647 by decadal-scale variability (e.g., Douglas, 1997). Furthermore, a 1-cm thick sample of sediment
648 from the uppermost part of the Placentia core represents ~20 years, which inhibits efforts to
649 reliably estimate RSL trends in the reconstruction on the same timescale as the tide gauge. The
650 data used to reconstruct RSL at Placentia are tabulated in the supporting information.

651

652 *4.4 Post-depositional lowering at Big River*

653 The physical and geotechnical properties of modern salt-marsh sediment were measured on 11
654 surface samples from Big River, Hynes Brook, and Placentia (Figure 8A–D; Table 2). This data
655 set provided empirical constraints on the relationship between organic content (measured by
656 LOI) and the parameters (voids ratio, recompression index, compression index, and specific
657 gravity) needed to run the decompaction model. High organic content is associated with
658 correspondingly high voids ratios, recompression index, and compression index, but lower
659 specific gravity. The nature of these relationships is similar to those observed on salt-marshes in
660 North Carolina (Brain et al., 2015), Connecticut (Brain et al., 2017), and the United Kingdom
661 (Brain et al., 2011; Brain et al., 2012) despite marked difference among these regions in climate,
662 salt-marsh vegetation, coastal geomorphology, and organic content of salt-marsh sediment.

In the Big River core, LOI varied from 13% to 70% (Figure 8F) and these values fall within the range measured on modern salt-marsh sediment in Newfoundland (12–82%). Samples with low LOI were typically comprised of thin and localized silt lenses. Measured dry bulk density was 0.10–0.47 g/cm^3, where the highest values occurred in the silt lenses (Figure 8G). Comparison of these values with those predicted by the decompaction model indicates a tendency for the model to modestly over predict the dry bulk density of the silt lenses (estimates of post-depositional lowering may subsequently be overestimated) in underlying sediments. However, given the low density and thin nature of these discontinuous lenses, we do not consider this effect to be significant in our post-depositional lowering estimates throughout the core. For all samples in the core, the relationship between measured and predicted dry density has an r^2 value of 0.52, and 88% of measured values lie within the 2σ predictions of the model (Figure 8E). Application of the geotechnical model to the Big River core shows that effective stress increases with depth from zero at the surface to ~3 kPa at 3.20 m, which yields estimates of post-depositional lowering that increase from zero at the top of the core to a characteristic peak in the middle of the core (less than 0.02 m), before decreasing once again to zero at the base of the core (Figure 8I). The magnitude of estimated post-depositional lowering through mechanical compression is similar to estimates generated elsewhere by applying geotechnical models to near-continuous sequences of high salt-marsh peat (Brain et al., 2015; Zoccarato and Teatini, 2017). Comparison of the Big River RSL reconstruction with a regional-scale database of basal (compaction-free) sea-level index points compiled by Love et al. (2016; Figure 5A) further suggests that the contribution of compaction was small. Based on these results, we contend that post-depositional lowering through physical compression is unlikely to have exceeded 0.02 m in the samples used

686 to reconstruct RSL at Placentia because the thicker sequence of peat at Big River is more prone
687 to this effect than the thinner sequence (~1.4 m) at Placentia. Compaction data are tabulated in
688 the supporting information for Big River.

689

690 **5. DISCUSSION**

691 *5.1 Decomposition of relative sea-level trends*

692 Although any single RSL reconstruction is necessarily and unavoidably representative of trends
693 at a specific location, regional- and global-scale trends can be investigated by analyzing a
694 multi-site network of reconstructions. We used the spatio-temporal empirical hierarchical model
695 (section 3.6) to decompose a global dataset of RSL reconstructions and co-located tide-gauge
696 measurements into contributions from processes characterized by different spatial and temporal
697 scales. The spatio-temporal model simultaneously analyzes each reconstruction and shares
698 information among sites to generate a posterior RSL history for each site. In agreement with the
699 original reconstructions, RSL estimated by the spatio-temporal model rose by ~3.0 m at Big
700 River over the past ~3000 years compared to ~1.5 m at Placentia (Figure 9). The
701 model-estimated RSL curves fall within the uncertainties of the original RSL reconstruction,
702 indicating that the underlying data is accurately represented by the model. Implicitly, the
703 spatio-temporal model assumes that each of the datasets provided as input are accurate
704 reconstructions of RSL. Therefore, variability within and among reconstructions is considered to
705 primarily be the result of physical processes rather than the choices (e.g., definitions of
706 standardized water level indexes, type of transfer function, and type of age-depth model) that
707 were made to produce the reconstructions.

708

709 At Big River and Placentia, most RSL rise during the past ~3000 years is attributed to
710 regional-scale linear processes (Figure 9) that we interpret primarily as GIA (e.g., Love et al.,
711 2016; Peltier, 2004) at a rate of 0.98 ± 0.05 mm/yr (95% credible interval) at Big River and 0.51
712 ± 0.05 mm/yr (95% credible interval) at Placentia. The rate of reconstructed, regional-scale
713 linear sea-level rise at Big River and Placentia is typically less than the rate inferred from RSL
714 predictions generated by the widely-used ICE-6G VM5 (Peltier et al., 2015) and ICE-5G VM2
715 (Peltier, 2004) Earth-ice models (Figure 5). Similar differences were noted in studies that
716 compared sea-level index points derived from salt-marsh sediment to RSL predictions from
717 Earth-ice models (e.g., Roy and Peltier, 2015).
718
719 The global-scale component of reconstructed RSL is largely consistent with the results of Kopp
720 et al. (2016). It varies by ~0.2 m and includes a gradual rise over 0–600 CE that was followed by
721 a marked fall from 1000 CE to 1200 CE (Figures 9 and 10A). Over the 20th century, global sea
722 level rose by 13.6 ± 1.4 mm/yr (95% credible interval), in agreement with global tide-gauge
723 compilations. However, this agreement is to be expected because the input data analyzed by the
724 spatio-temporal model included the global tide gauge record of Hay et al. (2015). This is the
725 fastest centennial-scale rate of rise in the past 3000 years ($P > 0.999$), which is a stronger
726 conclusion than the equivalent analysis of Kopp et al. (2016), who found that the 20th century
727 rise was extremely likely ($P = 0.95$) faster than during any century since at least –800 CE.
728
729 *5.2 Local-scale contribution*
730 The estimated contribution from local-scale processes to RSL trends along the Atlantic coast of
731 North America is typically less than ± 5 cm (Figure 10B). This interpretation is also partly

supported by geotechnical modeling, which showed that post-depositional lowering through sediment compaction (a commonly invoked local-scale process) was minimal at Big River (Figure 8) and probably also at Placentia. A comparison of basal (compaction-free) sea-level index points from western Newfoundland (Love et al., 2016) with the Big River RSL reconstruction confirms that sediment compaction was not a major driver of reconstructed RSL change in Newfoundland (Figure 5). Work in Connecticut and North Carolina also concluded that compaction made a minimal contribution to RSL reconstructions generated from continuous sequences of high salt-marsh peat (Brain et al., 2017; Brain et al., 2015; Kemp et al., 2015; Zoccarato and Teatini, 2017).

Salt marshes on the open coast with simple geomorphologies and that continuously accumulated sediment in (near-)equilibrium with rising sea-level are ideal sites for reconstructing RSL. In practice sediment accumulation and preservation often favors sheltered, low-energy salt marshes. This is the case in eastern Newfoundland (e.g., Placentia), where salt marshes are rare and restricted to back-barrier settings. Placentia's geomorphology makes it potentially vulnerable to local-scale RSL variability (Figure 1E). For example, closure of the North Arm would isolate the site from astronomical tides and RSL trends in the ocean, while opening of the South Arm could increase marine influence and tidal range. However, the estimated contribution from local-scale processes to RSL at Placentia is not markedly larger than at Big River (Figure 9), or indeed other sites along the Atlantic coast of North America (Figure 10B). This result does not mean that local-scale processes were unimportant, only that they are not necessary to explain the observations (i.e. the original RSL reconstruction) within their uncertainty. For example, at Placentia the period ~1500–1800 CE (Figure 9) is characterized by variable and uncertain

reconstructions that could readily accommodate additional local-scale contributions with a magnitude of centimeters to tens of centimeters and a duration of decades to centuries. Such large values do not appear within the uncertainty envelope of the modeled, local-scale estimate at Placentia because there is no site in the database that requires such large local-scale contributions to explain the reconstructions within their uncertainty, and so the trained model does not find them parsimonious.

The Atlantic coast of North America has the greatest concentration of detailed RSL reconstructions spanning the past ~3000 years of any coastline in the world, but even here the network of available data remains sparse with individual records often separated by 100s of kilometers (Figure 1A). Due to the tendency for research to explore RSL variability among rather than within coastal regions, a single region (i.e., a geographic area with a shared climate and oceanographic regime) may have only a handful of reconstructions and often only a single record. This geographic scarcity of data is a major challenge for efforts to separate regional-scale contributions that could reflect key climate-driven processes, such as changes in ocean or atmospheric circulation, from those that are restricted to a single core or site (local-scale processes). The characteristic scales of the regional non-linear and local contributions in the spatio-temporal model are 6.1° (~700 km) and 0.05° (<6 km) respectively (Table 3). Given the current distribution of neighboring RSL reconstructions compared to these scales (e.g., ~430 km from Big River to Placentia; ~700 km from Nassau Landing in Florida to Tump Point in North Carolina; Figure 1A), we acknowledge that robustly distinguishing between regional- and local-scale processes is a considerable challenge and is likely to be refined as additional reconstructions become available. Increased reconstruction precision will also help to

778 differentiate between contributions from regional- and local-scale processes because larger errors
779 allow the spatial temporal model to produce a posterior RSL history that is consistent with the
780 underlying data with only a modest contribution from local-scale processes.
781
782 *5.3 Regional-scale non-linear contribution*
783 The contrasting accumulation histories of Big River and Placentia (Figures 3 and 5) indicate that
784 the sites may have different fidelity in recording RSL changes. Big River is an example of an
785 ideal, continuously accumulating sequence, while the more complex history of sedimentation at
786 Placentia includes a ~1100-year period of little accumulation (Figure 5B). During this interval
787 assemblages of foraminifera (Figure 7; section 4.3) indicate a stable (and uniformly high)
788 paleo-marsh elevation, meaning that the RSL reconstruction is essentially equal to the
789 accumulation (age-depth) curve. At face value (and given only a small contribution from
790 local-scale processes), this implies that modest (~0.5 mm/yr), GIA-driven RSL rise was offset by
791 a regional, non-linear sea-level fall from ~0 to ~1100 CE. The resulting period of stable RSL
792 would cause the Placentia salt marsh to cease accumulating sediment, but continued tidal
793 inundation supported an *in-situ* population of foraminifera and prevented test loss through
794 desiccation.
795
796 A similar regional non-linear sea-level fall occurred at Big River, but ended several centuries
797 earlier than at Placentia (Figure 11A). The difference between the two reconstructions is greatest
798 at ~100–400 CE, perhaps because the lower rate of GIA at Placentia did not create sufficient
799 accommodation space to fully record the regional non-linear fall. In contrast, regional non-linear
800 trends at Big River and Placentia are essentially identical when Placentia is unambiguously

accumulating sediment. Notably the sites in the northeastern United States where background rates of GIA are relatively high (Figure 11B) display more coherence in the regional non-linear signal than sites in the southeastern United States (Figure 11C) where rates of GIA are relatively low, which further suggests that locations where accommodation space is created more rapidly have greater fidelity in recording regional non-linear sea-level changes.

Comparison of the regional non-linear component of RSL change during the past ~3000 years along the Atlantic coast of North America reveals three latitudinal groups of sites that share common trends (Figure 11). Sites in Atlantic Canada experienced a declining contribution from ~7 cm at –750 CE to a minimum of approximately –10 cm at 1000 CE, which was followed by an increase until ~1850 CE, after which the regional non-linear contribution declined slightly (Figure 1A). In the northeastern United States, regional non-linear sea level fell from ~8 cm at –1000 CE to a minimum of approximately –8 cm 400 CE (Figure 11B). It then remained stable until ~1200 CE, declined modestly until 1600 CE, and rose until present. In the southeastern United States (Figure 11C), regional non-linear sea level fell also fell from –1000 CE until ~500 CE when a period of stability began. The period 1000–1500 CE is characterized by a ~10 cm oscillation after which regional non-linear sea level rose to present. Studies of tide-gauge data noted similar spatial structure in sea-level trends, at least on annual to decadal timescales (e.g., McCarthy et al., 2015; Meade and Emery, 1971; Sallenger et al., 2012). We examine physical processes that could contribute to the coherent pattern of regional, non-linear sea-level trends presented in Figure 11.

823 Each of the three regions exhibits a sustained sea-level fall in the period preceeding ~500 CE
824 although the magnitude and rate of this trend varies among regions (Figure 11) and is
825 greatest/fastest in the southeastern United States. Over increasingly long periods of time, the
826 assumption that GIA is a linear process becomes weaker because the GIA process is slowing
827 down over multi-millennial timescales during the Holocene (e.g., Clark et al., 1978). The falling
828 sea-level trend, however, is not an effect of this non-linearity of GIA because this would produce
829 an early regional-scale sea-level rise that is larger at locations where the rate of GIA is faster. We
830 therefore, hypothesize that long-term cooling from the early to mid-Holocene maxima (e.g.,
831 Marcott et al., 2013; Marsicek et al., 2018) caused a corresponding (falling) steric sea-level
832 change. Observational data indicate that steric effects can produce a complex pattern of
833 regional-scale sea-level trends (e.g., Roemmich and Gilson, 2009; Willis et al., 2004). Therefore,
834 it is physically plausible that the trend is considered a regional rather than global trend by the
835 spatio-temporal model.
836
837 Since ~500 CE, the three regions show different regional non-linear sea-level trends (Figure 11).
838 Changes in the volume of the Greenland Ice Sheet would produce a characteristic fingerprint of
839 sea-level change (e.g., Clark and Lingle, 1977; Hay et al., 2014; Mitrovica et al., 2011) where
840 distal locations experience a larger sea-level change than locations closer to the ice sheet. For
841 example, the ratio of RSL change to global mean sea-level change caused by a uniform loss of
842 mass from the Greenland Ice Sheet is 0.7 at Fernandina Beach in northeastern Florida, 0.4 at
843 New London, Connecticut, and 0.0 at Argentia, Newfoundland (Kopp et al., 2014). The
844 latitudinal distribution of available RSL reconstructions is therefore well suited to identifying the
845 contribution (if sufficiently large) to RSL changes from the evolving mass of the Greenland Ice

846 Sheet. However, the characteristic and tell-tale fingerprint was not detected in our analysis
847 (Figure 11D). Although the behavior of the Greenland Ice Sheet during the past ~3000 years is
848 not well constrained (Alley et al., 2010), it likely advanced in response to cooling temperatures
849 (e.g., Marcott et al., 2013; PAGES2k, 2017) to reach a peak in mass and size at the end of the
850 Little Ice Age (Weidick et al., 2004). For example, Long et al. (2012) interpreted RSL rise
851 reconstructed in central west Greenland as evidence for growth of the Greenland Ice Sheet from
852 1300 CE to 1600 CE (these RSL reconstructions are included in the dataset analyzed using the
853 spatio-temporal model). Melting of the Greenland Ice Sheet since the end of the Little Ice Age
854 (~1850 CE) returned mass to the global ocean, although Long et al. (2012) propose that a slower
855 rate of RSL rise since 1600–1750 CE could indicate that mass loss began earlier. The fingerprint
856 of recent and accelerating mass loss is detectable on annual timescales in recent GRACE data
857 (Hsu and Velicogna, 2017). However, detailed analysis of 20th century tide-gauge data along the
858 U.S. Atlantic coast concluded that no fingerprint of Greenland Ice Sheet melt could be detected
859 (Piecuch et al., Accepted) as did studies that compared long-term rates of RSL rise to those
860 measured by nearby tide gauges (Engelhart et al., 2011). We therefore conclude that
861 regional-scale, non-linear sea-level trends during the past ~3000 years in the Western North
862 Atlantic Ocean cannot be adequately attributed to changes in the mass of the Greenland Ice Sheet
863 because the changes were too small and/or overprinted by contributions from other processes.
864
865 Redistribution of existing ocean mass by changes in the position and or/strength of prevailing
866 winds and ocean currents can cause dynamic sea-level trends that are regional in scale and act
867 over timescales from seasons to at least decades. For example, RSL observations from tide
868 gauges coupled with measurements of northward ocean transport at 26 °N from the RAPID array

869 (e.g., Bryden et al., 2005; Cunningham et al., 2007; McCarthy et al., 2012) indicated that a 30%
870 reduction of ocean transport (from 18.5 Sv to 12.8 Sv) caused by wind forcing and stronger
871 geostrophic flow over the winter of 2009–2010 led to sea-level rise north of Cape Hatteras
872 (Goddard et al., 2015). On decadal timescales, McCarthy et al. (2015) used the difference in
873 measured sea-level trends at sites to the north and south of Cape Hatteras (Figure 1A) as an
874 index of the strength of ocean circulation during the 20th century. These short timeseries of direct
875 observations and modeling studies indicate a relatively large range of coastal sea-level sensitivity
876 along the Atlantic coast of North America to changes in meridional ocean circulation (cm/Sv;
877 e.g., Bingham and Hughes, 2009; Ezer, 2016; Kuhlbrodt et al., 2007; Levermann et al., 2005).
878 Our results show that there was little difference in regional non-linear sea-level trends to the
879 north and south of Cape Hatteras for the period since ~1600 CE, which suggests that changes in
880 ocean circulation were too short-lived and/or small to cause a corresponding change in sea level
881 that was recorded by coastal sediment. In contrast, sea-level trends during the period from ~1000
882 CE to ~1500 CE do exhibit a notable difference between the northeastern and southeastern
883 United States (Figure 11). At sites south of Cape Hatteras sea level rose at 1000–1200 CE and
884 then fell to ~1500 CE. This oscillation was not recorded at locations north of Cape Hatteras,
885 which is suggestive of a contribution from ocean dynamics. However, recent proxy,
886 instrumental, and modeling studies also show that AMOC strength was stable until pronounced
887 weakening in the 20th century (Caesar et al., 2018; Thornalley et al., 2018). Furthermore, the
888 magnitude (~0.1 m) and duration (multiple centuries) of the sea-level difference would require a
889 correspondingly pronounced change in AMOC strength and may not be physically plausible,
890 unless it was associated (cause or effect) with an amplifying process such as shifts in prevailing
891 winds. There is some evidence that prevailing patterns of atmospheric circulation varied during

892 the past ~2000 years from proxy reconstructions of the North Atlantic Oscillation (e.g., Franke et
893 al., 2017; Ortega et al., 2015; Trouet et al., 2009). Although these reconstructions contradict one
894 another at certain times, there is also some agreement among records that a positive phase of the
895 North Atlantic Oscillation was sustained over the period of approximately 1100–1400 CE, which
896 broadly coincides with the noted differences in sea-level trends among regions on the Atlantic
897 coast of North America. However, similar spatial patterns of sea-level change are not present at
898 other times of sustained positive phases in the North Atlantic Oscillation (e.g., 450–750 CE).
899 Importantly, the relationship between the state of the North Atlantic Oscillation and RSL on the
900 Atlantic coast of North America (particularly as expressed by the difference between sites
901 located to the north and south of Cape Hatteras) is observed to vary depending on the timescale
902 and specific time window under consideration (Kenigson et al., 2018; McCarthy et al., 2015;
903 Piecuch et al., 2016; Woodworth et al., 2017). Furthermore, Woodworth et al. (2017) highlighted
904 differences in the response of the open, shelf, and coastal oceans to changing North Atlantic
905 Oscillation, which complicates understanding of how variability in the North Atlantic Ocean is
906 (or indeed is not) translated physically into sea-level variability. Deciphering the role of ocean
907 and atmospheric circulation as drivers of sea-level change (particularly during the past ~1000
908 years) is an avenue for future work that will likely require a higher density network of RSL
909 reconstructions than is currently available.
910
911 **6. CONCLUSIONS**
912 Newfoundland is likely one of the most northerly locations in the western Atlantic Ocean where
913 salt-marsh sediment records RSL rise during the past ~3000 years. It is therefore an important
914 region for reconstructing RSL to better understand the role of regional-scale, non-linear

processes as drivers of RSL change. We reconstructed RSL using foraminifera and testate amoebae preserved in cores of salt-marsh sediment at Big River and Placentia that were dated using radiocarbon and recognition of pollution horizons of known age and origin. Since approximately –1000 CE, RSL rose by ~3.0 m at Big River and ~1.5 m at Placentia. Results from a geotechnical model indicate that sediment compaction was minimal and therefore not a primary driver of RSL trends. We used a spatio-temporal model to decompose these RSL reconstructions (alongside those in an expanded Common Era database) into contributions from global, regional linear, regional non-linear, and local processes. The global contribution confirms that the 20th century rate of rise was the fastest century-scale trend of the past 3000 years. Most of the reconstructed RSL rise in Newfoundland is attributed to GIA. Only small local-scale contributions are needed to reconcile RSL reconstructions and denoised RSL trends, although larger contributions (particularly of short duration) can be accommodated within the RSL records and Placentia in particular may have experienced larger local-scale trends than we estimate. Regional non-linear sea-level in the western North Atlantic Ocean displays spatially- and temporally-coherent trends that enabled us to recognize three groups of sites (Canada, North of Cape Hatteras, and South of Cape Hatteras). Trends within and among these groups indicate that redistribution of existing ocean mass by ocean currents and/or winds likely contributed to reconstructed RSL trends.

ACKNOWLEDGEMENTS

This paper is dedicated to the memory of Orson van de Plassche and Alan Kemp. We thank Prof. Jerry Mitrovica for providing the GIA predictions for our study sites and Dr. Gerard McCarthy for discussions about AMOC variability across different timescales and two reviewers for

938 providing comments and suggestions that improved the paper. This work was supported by NSF
939 award OCE-1458921 to Kemp, by NSF award OCE-1458904 to Horton and Kopp, and by NSF
940 award OCE-1702587 and OCE-1804999 to Kopp. Foraminiferal data from Big River were
941 collected as part of a series of projects including "*Ocean-climate variability and sea level in the*
942 *North Atlantic region since AD 0*" funded by the Dutch National Research Program on Global air
943 pollution and Climate Change, "*Coastal Records*" funded by Vrije Universiteit Amsterdam, and
944 "*Simulations, observations & palaeoclimatic data: climate variability over the last 500 years*"
945 funded by the European Union. This is a contribution to IGCP project 639 "*Sea-level change*
946 *from minutes to millennia*" and PALSEA 2.

948 **TABLE 1:** Reported radiocarbon ages from the Big River (F25) and Placentia (C106) cores.
949

Core	Depth (cm)	Radiocarbon Age	Radiocarbon Age Error	$\delta^{13}C$ (‰, PDB)	Laboratory Number	Dated Material
Big River F25	16	76	29	–12.3	UtC–10372	Sp
Big River F25	24	143	41	–12.3	UtC–10373	Sp
Big River F25	32	176	31	–12.8	UtC–10374	Sp
Big River F25	40	125	39	–26.0	UtC–10375	Cr
Big River F25	48	125	35	–26.4	UtC–10376	Cr
Big River F25	54	233	26	–13.2	UtC–10517	Sp
Big River F25	60	286	33	–26.5	UtC–10516	Cr
Big River F25	66	332	34	–26.8	UtC–10515	Cr
Big River F25	74	367	33	–12.7	UtC–10470	Sp
Big River F25	80	415	40	–12.1	UtC–10518	Sp
Big River F25	86	530	34	–13.1	UtC–10519	Sp
Big River F25	94	546	42	–13.6	UtC–10520	Sp
Big River F25	102	263	29	–28.1	UtC–10521	Tm
Big River F25	107	846	38	–26.2	UtC–10522	Cr
Big River F25	108	837	36	–27.8	UtC–10523	Tm
Big River F25	119	1039	38	–13.8	UtC–10524	Sp
Big River F25	125	1012	38	–27.2	UtC–10525	Tm
Big River F25	133	1111	30	–27.1	UtC–10526	Tm
Big River F25	141	1243	39	–12.1	UtC–10527	Sp
Big River F25	149	1323	36	–25.6	UtC–10528	Tm
Big River F25	157	1321	31	–27.7	UtC–10529	Sr
Big River F25	166	1508	31	–27.9	UtC–10471	Sr
Big River F25	174	1643	29	–11.8	UtC–10472	Sp
Big River F25	174	1597	28	–15.0	UtC–10473	Sp
Big River F25	182	1653	29	–12.5	UtC–10474	Sp
Big River F25	189	1684	30	–26.6	UtC–10475	Sp
Big River F25	190	1722	31	–26.2	UtC–10476	Cr
Big River F25	195	1782	29	–13.1	UtC–10477	Sp
Big River F25	203	1842	28	–14.1	UtC–10478	Sp
Big River F25	208	1892	36	–27.8	UtC–10479	Sr
Big River F25	214	1944	30	–26.5	UtC–10480	Cr
Big River F25	220	1909	32	–27.5	UtC–10481	Tm
Big River F25	229	2017	30	–27.2	UtC–10482	Sr
Big River F25	235	2168	31	–26.5	UtC–10483	Tm
Big River F25	245	2234	33	–26.8	UtC–10484	Tm
Big River F25	254	2359	39	–27.7	UtC–10485	Tm
Big River F25	261	2422	35	–28.6	UtC–10486	Sr
Big River F25	267	2492	38	–12.9	UtC–10441	Sr
Big River F25	271	2470	43	–28.5	UtC–10442	Sr
Big River F25	277	2481	38	–26.3	UtC–10502	Tm
Big River F25	285	2578	40	–27.7	UtC–10398	Sr
Big River F25	291	2705	41	–27.5	UtC–10399	Sr
Placentia C106	30	295	20	–25.77	OS–123338	Woody rhizome
Placentia C106	30	155	20	–25.83	OS–123569	Woody rhizome
Placentia C106	30	215	15	–25.45	OS–123880	Woody rhizome
Placentia C106	39	495	15	–28.07	OS–122235	Woody rhizome
Placentia C106	45	565	20	–28.94	OS–123342	Woody rhizome
Placentia C106	45	550	20	–29.07	OS–123570	Woody rhizome
Placentia C106	51	520	15	–28.55	OS–120939	Woody rhizome
Placentia C106	60	605	20	–26.80	OS–122236	Woody rhizome
Placentia C106	64	625	25	–27.92	OS–123341	Woody rhizome
Placentia C106	77	890	20	–27.00	OS–122237	Woody rhizome
Placentia C106	80	1740	20	–24.95	OS–120940	Woody rhizome
Placentia C106	83	950	25	–27.77	OS–123340	Wood fragments
Placentia C106	89	1500	20	–26.27	OS–123339	Wood fragments

Placentia C106	94	1730	20	–26.83	OS–120941	Woody rhizome
Placentia C106	95	1910	20	–13.23	OS–122238	Ds
Placentia C106	102	2060	20	–12.65	OS–122239	Ds
Placentia C106	109	2200	20	–12.84	OS–120942	Ds
Placentia C106	118	2240	20	–25.02	OS–122240	Woody rhizome
Placentia C106	127	2220	20	–13.40	OS–120981	Ds
Placentia C106	132	2330	20	–12.11	OS–123306	Ds
Placentia C106	136	2430	20	–12.44	OS–120982	Ds
Placentia C106	141	2480	20	–23.91	OS–123337	Woody rhizome
Placentia C106	141	2470	20	–24.01	OS–123571	Woody rhizome

Reported radiocarbon ages for samples in the Big River and Placentia cores. Samples identified by the prefix "UtC" were dated at the Utrecht van der Graaf Laboratorium. The reported radiocarbon ages and errors (1σ) from this laboratory were not rounded following the conventions of Stuiver and Polach (1977). Samples identified by the prefix "OS" were dated at the U.S. National Ocean Sciences Accelerator Mass Spectrometry laboratory and reported ages and (1σ) errors were rounded following the conventions of Stuiver and Polach (1977). Sample $\delta^{13}C$ values are provided relative to the Pee Dee Belemnite (PDB) standard. Sample depths listed in table include a 2-cm adjustment for dating of plant remains that lived beneath the paleo salt-marsh surface. In the Placentia core, the samples at depths of 30 cm, 45 cm, and 141 cm were dated more than once as part of a quality control procedure at the NOSAMS facility. The ages represented repeated measurements on the same plant sample and we therefore incorporated these dates into the age-depth model after creating a pooled mean for each of the three depths with replicate radiocarbon measurements. Samples described as woody rhizomes were not identified to the species level. Sp = *Spartina patens*, Cr = *Carex rostrata*, Tm = *Triglochin maritima*, Sr = *Scirpus robustus,* Ds = *Distichlis spicata*.

966 **Table 2:** Physical and geotechnical properties of modern salt-marsh sediment in Newfoundland.
967

Sample ID	Loss-on-ignition, LOI (%)	Particle density, G_s	Voids ratio at 1 kPa, e_1	Recompression index, C_r	Compression index, C_c	Yield stress, σ'_y (kPa)
BRB15/ST06	24.05	2.42	5.69	0.07	0.83	10.5
BRM15/ST09	24.35	2.33	7.57	0.09	1.78	4
HBM15/ST02	13.88	2.75	3.23	0.04	0.93	3
HBM15/ST05	24.61	2.53	4.96	0.06	1.06	5
HBM15/ST06	32.52	2.13	5.52	0.044	1.64	4
HBM15/ST07	37.33	2.29	9.82	0.076	3.26	3
HBM15/ST09	40.00	2.08	10.08	0.12	1.32	11.5
HBM15/ST011	23.16	2.34	6.37	0.09	1.9	4
HBM15/ST013	12.32	2.57	4.15	0.02	1.56	6
PAL15/C/ST08	68.28	2.06	12.21	0.17	4.19	7
PAL15/B/ST12	81.72	1.98	16.93	0.32	2.97	8

968 The recompression index, C_r, describes the compressibility of the sample in its pre-yield, reduced
969 compressibility condition. The compression index, C_r, describes the compressibility of the
970 sample its post-yield, increased-compressibility condition. The yield stress, σ'_y, defines the
971 transition from reduced- to increased-compressibility states.
972
973

974 **Table 3. Optimized hyperparameters for spatio-temporal empirical hierarchical model**
975

Term	Prior SD	Characteristic Timescale (years)	Characteristic Length Scale (Degrees)
$g_f(t)$ [fast global]	± 0.2 cm	12	–
$g_s(t)$ [slow global]	± 16 cm	326	
$m(\mathbf{x})$ [linear]	± 1.1 mm/yr	–	4.7
$r_f(\mathbf{x},t)$ [fast regional]	± 2 cm	12	6.1
$r_s(\mathbf{x},t)$ [slow regional]	± 6 cm	326	6.1
$l_f(\mathbf{x},t)$ [fast local]	± 2 cm	12	0.05
$l_s(\mathbf{x},t)$ [slow local]	± 3 cm	326	0.05
$w(\mathbf{x},t)$ [additional error]	± 0.02 mm	–	–
$y_0(\mathbf{x})$ [datum offset]	± 0.1 mm	–	–

976

977 **FIGURE CAPTIONS**

978

979 **Figure 1: (A)** Location of study sites in Newfoundland, Canada and existing, high-resolution
980 relative sea-level reconstructions from the Atlantic coast of North America. Dashed line marks
981 the approximate hinge line separating locations experiencing recent uplift/subsidence (RSL
982 fall/rise) caused by glacio-isostatic adjustment. Location of the Port-aux-Basques and Argentia
983 tide gauges are shown. **(B–F)** Site maps showing locations of coring transects and surface
984 transects that provided samples to characterize the modern distribution of foraminifera, testate
985 amoebae (Kemp et al., 2017c; Wright et al., 2011), and the geotechnical properties of modern
986 sediment (this study). **(G–J)** Simplified stratigraphy beneath the salt marshes at Big River and
987 Placentia. At Big River, core F25 was selected for detailed analysis. At Placentia, core 106 was
988 selected for detailed analysis.

989

990 **Figure 2:** 10-fold cross validation of the Bayesian transfer functions. Left column shows results
991 for foraminifera, symbol shading denotes site. Right column shows results for testate amoebae;
992 samples from Newfoundland are represented by circles (Kemp et al., 2017c) shaded to denote
993 sites; samples from the North Atlantic dataset of Barnett et al. (2017b) are represented by squares
994 shaded to denote region. Top row shows actual elevation (measured at the time of sample
995 collection) and elevation predicted under cross validation by the transfer function. Vertical error
996 bars show the 95% credible interval of predicted elevation. Dashed 1:1 lines are provided for
997 reference. Bottom row is the residual (difference) between actual and predicted elevations. All
998 elevations are expressed as a standardized water level index. For foraminifera, a standardized
999 water level index (F-SWLI) of 100 is local mean tide level (MTL) and a value of 200

corresponds to the highest occurrence of foraminifera (HOF). For testate amoebae a standardized water level index (T-SWLI) of 0 is the lowest occurrence of testate amoebae (LOT) and a value of 100 corresponds to highest astronomical tide (HAT).

Figure 3: Big River chronology. **(A)** Downcore profiles of ^{137}Cs, Pb isotopes (^{206}Pb:^{207}Pb), and Pb concentration used to recognize marker horizons of known age. Shaded depths show the interval in the core that corresponds to each horizon and were included in the age-depth model as a sampling uncertainty. Labeled ages list the age assigned to each horizon and the uncertainty was included in the age-depth model with a uniform probability distribution. **(B)** Age-depth model developed for the Big River core using Bchron. Shaded envelope is the 95% credible interval summarized from a suite of equi-probable accumulation histories. Symbols represent marker horizons (uncertainties are smaller than symbols). Radiocarbon ages are calibrated ages with bar thickness proportional to probability (note that a single radiocarbon age often yields multiple calibrated ranges; thicker bar denotes higher probability). **(C)** Mean annual rate of sediment accumulation estimated using the Bchron age-depth model, solid line represents mean rate and shaded envelope captures the 5^{th}–95^{th} percentiles.

Figure 4: Assemblages of foraminifera in the Big River core. Abundance of the five most common taxa are presented and together these taxa made up 99.6% of all counted individuals. Jm = *Jadammina macrescens*; BP = *Balticammina pseudomacrescens*; Tc = *Tiphotrocha comprimata*; Hs = *Haplophragmoides* spp.; Ti = *Trochammina inflata*; Mf = *Miliammina fusca*. Samples yielding fewer than 50 individual foraminifera (shaded circles) were excluded from the final relative sea-level reconstruction. The dissimilarity between each sample in the core and its

closest modern analog was measured using the Bray-Curtis distance metric. If measured dissimilarity exceeded the 20th percentile of dissimilarity among all possible pairs of modern samples (labeled and dashed vertical line; the 10th and 5th percentiles are also shown for reference) the sample was excluded from the final relative sea-level reconstruction. Symbol shading denotes the site in the modern training set that provided the closest modern analog. Application of the Bayesian transfer function yielded reconstructions of paleomarsh elevation in standardized water level index (F-SWLI) units, where a value of 100 corresponds to mean tide level (MTL) and 200 is the highest occurrence of foraminifera (HOF) in the modern training set. Sample-specific uncertainties are the 95% credible interval.

Figure 5: Relative sea-level reconstructions from Big River and Placentia. Each box represents the vertical and chronological uncertainty of a single data point. Predictions from two widely used Earth-ice models (ICE-6G VM5; Argus et al., 2014 and ICE-5G VM2 ; Peltier, 2004) are shown for comparison. For Big River, discrete, independent, and previously published relative sea-level reconstructions from sites in western Newfoundland are show as blue boxes (Love et al., 2016) that represent vertical and chronological uncertainty.

Figure 6: Placentia chronology. **(A)** Downcore profiles of ^{137}Cs, Pb isotopes (^{206}Pb:^{207}Pb), and Pb, V and Cu concentrations used to recognize marker horizons of known age. Shaded depths show the interval in the core that corresponds to each horizon and were included in the age-depth model as a sampling uncertainty. Labeled ages list the age assigned to each horizon and the uncertainty was included in the age-depth model with a uniform probability distribution. **(B)** Age-depth model developed for the Placentia core using Bchron. Shaded envelope is the 95%

credible interval summarized from a suite of equi-probable accumulation histories. Symbols represent marker horizons (uncertainties are smaller than symbols). Radiocarbon ages are calibrated ages with bar thickness proportional to probability (note that a single radiocarbon age often yields multiple calibrated ranges). For reference, the depths at which foraminifera were sparse or absent are highlighted. **(C)** Mean annual rate of sediment accumulation estimated using the Bchron age-depth model, solid line represents mean rate and shaded envelope captures the 5^{th}–95^{th} percentiles.

Figure 7: Assemblages of foraminifera (red) and testate amoebae (blue) in the Placentia core. Abundance of the two most common taxa of foraminifera are presented and together comprise 98.6% of individuals across all samples. Jm = *Jadammina macrescens*; Bp = *Balticammina pseudomacrescens*; Ti = *Trochammina inflata*. Paleomarsh elevation (PME) was reconstructed from the assemblages of foraminifera using a Bayesian transfer function (error bars represent the 95% credible interval) and is expressed as a standardized water level index (F-SWLI) where a value of 200 is equal to the highest occurrence of foraminifera (HOF). Abundance of the three most common taxa of testate amoebae are presented and together comprise 58.2% of individuals across all samples. Ce.ac.t = *Centropyxis aculeata* type; Ce.ca.t = *Centropyxis cassis* type; Ps.t = *Psudocorythion* type. PME was reconstructed from assemblages of testate amoebae using a Bayesian transfer function and is expressed as a standardized water level index (T-SWLI) where a value of 0 is equal to the lowest occurrence of testate amoebae (LOT) and a value of 200 is highest astronomical tide (HAT). In this panel HOF is also shown for comparison following correction for the difference in standardization between datasets. Dissimilarity between each core sample and its closest modern analog was measured using the Bray Curtis distance metric.

Samples with a minimum dissimilarity less than the 20th percentile measured among all possible pairings of samples (dashed and labeled vertical lines; the 10th and 5th percentiles are also shown for comparison) in the modern training sets are deemed to have an appropriate analogue.

Figure 8: Estimation of post-depositional lowering caused by physical compression of core sediment. **(A–D)** Observed relationships between organic content (measured using loss-on-ignition; LOI) and geotechnical/physical properties of modern salt-marsh sediments collected from Big River, Hynes Brook, and Placentia (distinguished by symbol shape and shading). Dashed lines (with equations) represent best fit, except in panel D where the equation and line are from Hobbs (1986). **(E)** Comparison of model-predicted and measured bulk density for sediment samples in the Big River core. Modeled values are the mean and standard deviation of 5000 model runs. **(F–I)** Measured (blue) and modeled (orange, mean and 95% credible interval) geotechnical/physical properties (including post-depositional lowering) of sediment samples in the Big River core. **(J)** Lithostratigrahy of the Big River core.

Figure 9: Decomposition of relative sea-level reconstructions from Newfoundland using a spatio-temporal model. In all cases, the solid line and shaded envelope are the model mean and 1σ uncertainty. The left column presents results from Big River and the right column presents results from Placentia. Rows are the estimated contribution to relative sea level from specific groups of physical processes. Axes are standardized across columns to aid comparison of Big River and Placentia. The vertical scale for the panels depicting relative sea level and the regional-scale linear component are the same. Likewise, the panels presenting global sea level

share a vertical scale with those presenting the combined contribution from regional, non-linear and local processes.

Figure 10: (A) Reconstructed global mean sea level (mean with 1σ uncertainty). **(B)** Contribution of local-scale trends to reconstructed relative sea level at sites along the Atlantic coast of North America. For ease of comparison, only select sites (colored in latitudinal order) and model means are shown. Geotechnical models estimate little or no contribution from sediment compaction at Big River, Newfoundland and the record from East River, Connecticut was generated entirely from compaction-free basal sediment.

Figure 11: (A–C) The regional-scale non-linear contribution to reconstructed relative sea level for three, latitudinally-organized regions along the Atlantic coast of North America. For ease of comparison, only select sites are shown. Each series is represented by a mean (solid line) and uncertainty (±1σ; shaded envelope). **(D–E)** Spatial pattern of mean, non-linear sea-level change estimated by the spatio-temporal model (units of mm/yr) for three time intervals. Note that scale differs among panels. CH = location of Cape Hatteras.

REFERENCES

Alley, R.B., Andrews, J.T., Brigham-Grette, J., Clarke, G.K.C., Cuffey, K.M., Fitzpatrick, J.J., Funder, S., Marshall, S.J., Miller, G.H., Mitrovica, J.X., Muhs, D.R., Otto-Bliesner, B.L., Polyak, L., White, J.W.C., 2010. History of the Greenland Ice Sheet: paleoclimatic insights. Quaternary Science Reviews 29, 1728-1756.

Argus, D.F., Peltier, W.R., Drummond, R., Moore, A.W., 2014. The Antarctic component of postglacial rebound model ICE-6G_C (VM5a) based upon GPS positioning, exposure age dating of ice thicknesses and relative sea level histories. Geophysical Journal International 198, 537-563.

Barnett, R.L., Bernatchez, P., Garneau, M., Juneau, M.N., 2017a. Reconstructing late Holocene relative sea-level changes at the Magdalen Islands (Gulf of St. Lawrence, Canada) using multi-proxy analyses. Journal of Quaternary Science 32, 380-395.

Barnett, R.L., Charman, D.J., Gehrels, W.R., Saher, M.H., Marshall, W.A., 2013. Testate amoebae as sea-level indicators in northwestern Norway: developments in sample preparation and analysis. Acta Protozoologica 52, 115-128.

Barnett, R.L., Newton, T.L., Charman, D.J., Gehrels, W.R., 2017b. Salt-marsh testate amoebae as precise and widespread indicators of sea-level change. Earth-Science Reviews 164, 193-207.

Bell, T., Daly, J.F., Batterson, M.J., Liverman, D.G., Shaw, J., Smith, I., 2005. Late Quaternary relative sea-level change on the West coast of Newfoundland. Géographie Physique et Quaternaire 59, 129-140.

Bingham, R.J., Hughes, C.W., 2009. Signature of the Atlantic meridional overturning circulation in sea level along the east coast of North America. Geophysical Research Letters 36, L02603.

Bloom, A.L., 1964. Peat accumulation and compaction in Connecticut coastal marsh. Journal of Sedimentary Research 34, 599-603.

Brain, M.J., 2016. Past, present and future perspectives of sediment compaction as a driver of relative sea level and coastal change. Current Climate Change Reports 2, 75-85.

Brain, M.J., Kemp, A.C., Hawkes, A.D., Vane, C.H., Cahill, N., Hill, T.D., Engelhart, S.E., Donnelly, J.P., Horton, B.P., 2017. The contribution of mechanical compression and biodegradation to compaction of salt-marsh sediments and relative sea-level reconstructions. Quaternary Science Reviews 167, 96-111.

Brain, M.J., Kemp, A.C., Horton, B.P., Culver, S.J., Parnell, A.C., Cahill, N., 2015. Quantifying the contribution of sediment compaction to late Holocene salt-marsh sea-level reconstructions, North Carolina, USA. Quaternary Research 83, 41-51.

Brain, M.J., Long, A.J., Petley, D.N., Horton, B.P., Allison, R.J., 2011. Compression behaviour of minerogenic low energy intertidal sediments. Sedimentary Geology 233, 28-41.

Brain, M.J., Long, A.J., Woodroffe, S.A., Petley, D.N., Milledge, D.G., Parnell, A.C., 2012. Modelling the effects of sediment compaction on salt marsh reconstructions of recent sea-level rise. Earth and Planetary Science Letters 345-348, 180-193.

Brookes, I., Scott, D., McAndrews, J., 1985. Postglacial relative sea-level change, Port au Port area, west Newfoundland. Canadian Journal of Earth Sciences 22, 1039-1047.

Bryden, H.L., Longworth, H.R., Cunningham, S.A., 2005. Slowing of the Atlantic meridional overturning circulation at 25 N. Nature 438, 655-657.

Caesar, L., Rahmstorf, S., Robinson, A., Feulner, G., Saba, V., 2018. Observed fingerprint of a weakening Atlantic Ocean overturning circulation. Nature 556, 191-196.

Cahill, N., Kemp, A.C., Parnell, A.C., Horton, B.P., 2016. A Bayesian hierarchical model for reconstructing relative sea level: from raw data to rates. Climate of the Past 12, 525-542.

Charman, D.J., Gehrels, W.R., Manning, C., Sharma, C., 2010. Reconstruction of recent sea-level change using testate amoebae. Quaternary Research 73, 208-219.

Charman, D.J., Hendon, D., Woodland, W.A., 2000. The Identification of Peatland Testate Amoebae. Quaternary Research Association, London.

Chillrud, S.N., Bopp, R.F., Simpson, H.J., Ross, J.M., Shuster, E.L., Chaky, D.A., Walsh, D.C., Choy, C.C., Tolley, L.-R., Yarme, A., 1999. Twentieth century atmospheric metal fluxes into Central Park Lake, New York City. Environmental Science & Technology 33, 657-662.

Church, J.A., Clark, P.U., Cazenave, A., Gregory, J.M., Jevrejeva, S., Levermann, A., Merrifield, M.A., Milne, G.A., Nerem, R.S., Nunn, P.D., Payne, A.J., Pfeffer, W.T., Stammer, D., Unnikrishnan, A.S., 2013. Sea-level change, in: Stocker, T.F., D. Qin, D., Plattner, G.K., Tignor, M., Allen, S.K., Boschung, J., Nauels, A., Xia, Y., Bex, V., Midgley, P.M. (Eds.), Climate Change 2013: The Physical Science Basis. Contribution of Working Group I to the Fifth Assessment Report of the Intergovernmental Panel on Climate Change. Cambridge University Press, pp. 1137-1216.

Clark, J.A., Farrell, W.E., Peltier, W.R., 1978. Global changes in postglacial sea level: A numerical calculation. Quaternary Research 9, 265-287.

Clark, J.A., Lingle, C.S., 1977. Future sea-level changes due to West Antarctic ice sheet fluctuations. Nature 269, 206-209.

Cox, T., 2016. Tides: Quasi-periodic time series characteristics, 1.2 ed.

Cunningham, S.A., Kanzow, T., Rayner, D., Baringer, M.O., Johns, W.E., Marotzke, J., Longworth, H.R., Grant, E.M., Hirschi, J.J.-M., Beal, L.M., 2007. Temporal variability of the Atlantic meridional overturning circulation at 26.5 N. Science 317, 935-938.

Daly, J.F., 2002. Late Holocene sea-level change around Newfoundland, Geological Sciences. University of Maine, p. 220.

Daly, J.F., Belknap, D.F., Kelley, J.T., Bell, T., 2007. Late Holocene sea-level change around Newfoundland. Canadian Journal of Earth Sciences 44, 1453-1465.

Doe, B.R., Delevaux, M.H., 1972. Source of lead in southeast Missouri galena ores. Economic Geology 67, 409-425.

Douglas, B.C., 1997. Global sea rise: a redetermination. Surveys in Geophysics 18, 279-292.

Edwards, R.J., Wright, A.J., 2015. Foraminifera, in: Shennan, I., Long, A.J., Horton, B.P. (Eds.), Handbook of Sea-Level Research. John Wiley & Sons, Chichester, pp. 191-217.

Engelhart, S.E., Horton, B.P., Douglas, B.C., Peltier, W.R., Tornqvist, T.E., 2009. Spatial variability of late Holocene and 20th century sea-level rise along the Atlantic coast of the United States. Geology 37, 1115-1118.

Engelhart, S.E., Peltier, W.R., Horton, B.P., 2011. Holocene relative sea-level changes and glacial isostatic adjustment of the U.S. Atlantic coast. Geology 39, 751-754.

Ezer, T., 2015. Detecting changes in the transport of the Gulf Stream and the Atlantic overturning circulation from coastal sea level data: The extreme decline in 2009–2010 and estimated variations for 1935–2012. Global and Planetary Change 129, 23-36.

Ezer, T., 2016. Can the Gulf Stream induce coherent short-term fluctuations in sea level along the US East Coast? A modeling study. Ocean Dynamics 66, 207-220.

Forbes, D., Orford, J., Carter, R., Shaw, J., Jennings, S., 1995. Morphodynamic evolution, self-organisation, and instability of coarse-clastic barriers on paraglacial coasts. Marine Geology 126, 63-85.

Franke, J.G., Werner, J.P., Donner, R.V., 2017. Reconstructing Late Holocene North Atlantic atmospheric circulation changes using functional paleoclimate networks. Climate of the Past 13, 1593.

Gehrels, W.R., Kirby, J.R., Prokoph, A., Newnham, R.M., Achterberg, E.P., Evans, H., Black, S., Scott, D.B., 2005. Onset of recent rapid sea-level rise in the western Atlantic Ocean. Quaternary Science Reviews 24, 2083-2100.

Gerlach, M.J., Engelhart, S.E., Kemp, A.C., Moyer, R.P., Smoak, J.M., Bernhardt, C.E., Cahill, N., 2017. Reconstructing Common Era relative sea-level change on the Gulf coast of Florida. Marine Geology 390, 254-269.

Gobeil, C., Tessier, A., Couture, R.-M., 2013. Upper Mississippi Pb as a mid-1800s chronostratigraphic marker in sediments from seasonally anoxic lakes in Eastern Canada. Geochimica et Cosmochimica Acta 113, 125-135.

Goddard, P.B., Yin, J., Griffies, S.M., Zhang, S., 2015. An extreme event of sea-level rise along the Northeast coast of North America in 2009–2010. Nature Communications 6, 6346.

Graney, J.R., Halliday, A.N., Keeler, G.J., Nriagu, J.O., Robbins, J.A., Norton, S.A., 1995. Isotopic record of lead pollution in lake sediments from the northeastern United States. Geochimica et Cosmochimica Acta 59, 1715-1728.

Haslett, J., Parnell, A., 2008. A simple monotone process with application to radiocarbon-dated depth chronologies. Journal of the Royal Statistical Society: Series C (Applied Statistics) 57, 399-418.

Hay, C., Mitrovica, J.X., Gomez, N., Creveling, J.R., Austermann, J., Kopp, R.E., 2014. The sea-level fingerprints of ice-sheet collapse during interglacial periods. Quaternary Science Reviews 87, 60-69.

Hay, C., Morrow, E., Kopp, R.E., Mitrovica, J.X., 2015. Probabilistic reanalysis of twentieth-century sea-level rise. Nature 517, 481-484.

Head, K.H., 2008. Manual of Soil Laboratory Testing: Soil Classification and Compaction Tests. Whittles, Caithness.

Head, K.H., Epps, R.J., 2011. Manual of Soil Laboratory Testing Volume II: Permeability, Shear Strength and Compressibility Tests. Whittles, Caithness.

Heyl, A.V., Delevaux, M.H., Zartman, R.E., Brock, M.R., 1966. Isotopic study of galenas from the upper Mississippi Valley, the Illinois-Kentucky, and some Appalachian Valley mineral districts. Economic Geology 61, 933-961.

Hill, T.D., Anisfeld, S.C., 2015. Coastal wetland response to sea level rise in Connecticut and New York. Estuarine, Coastal and Shelf Science 163, Part B, 185-193.

Hobbs, N., 1986. Mire morphology and the properties and behaviour of some British and foreign peats. Quarterly Journal of Engineering Geology and Hydrogeology 19, 7-80.

Holgate, S.J., Matthews, A., Woodworth, P.L., Rickards, L.J., Tamisiea, M.E., Bradshaw, E., Foden, P.R., Gordon, K.M., Jevrejeva, S., Pugh, J., 2013. New data systems and products at the Permanent Service for Mean Sea Level. Journal of Coastal Research 29, 493-504.

Hsu, C.W., Velicogna, I., 2017. Detection of sea level fingerprints derived from GRACE gravity data. Geophysical Research Letters 44, 8953-8961.

Jackson, S.T., Williams, J.W., 2004. Modern analogs in Quaternary paleoecology: here today, gone yesterday, gone tomorrow? Annual Review of Earth and Planetary Sciences 32, 495-537.

Keigwin, L.D., Boyle, E.A., 2000. Detecting Holocene changes in thermohaline circulation. Proceedings of the National Academy of Sciences 97, 1343-1346.

Kemp, A.C., Bernhardt, C.E., Horton, B.P., Vane, C.H., Peltier, W.R., Hawkes, A.D., Donnelly, J.P., Parnell, A.C., Cahill, N., 2014. Late Holocene sea- and land-level change on the U.S. southeastern Atlantic coast. Marine Geology 357, 90-100.

Kemp, A.C., Hawkes, A.D., Donnelly, J.P., Vane, C.H., Horton, B.P., Hill, T.D., Anisfeld, S.C., Parnell, A.C., Cahill, N., 2015. Relative sea-level change in Connecticut (USA) during the last 2200 years. Earth and Planetary Science Letters 428, 217-229.

Kemp, A.C., Hill, T.D., Vane, C.H., Cahill, N., Orton, P., Talke, S.A., Parnell, A.C., Sanborn, K., Hartig, E.K., 2017a. Relative sea-level trends in New York City during the past 1500 years. The Holocene.

Kemp, A.C., Horton, B.P., Vane, C.H., Corbett, D.R., Bernhardt, C.E., Engelhart, S.E., Anisfeld, S.C., Parnell, A.C., Cahill, N., 2013. Sea-level change during the last 2500 years in New Jersey, USA. Quaternary Science Reviews 81, 90-104.

Kemp, A.C., Kegel, J.J., Culver, S.J., Barber, D.C., Mallinson, D.J., Leorri, E., Bernhardt, C.E., Cahill, N., Riggs, S.R., Woodson, A.L., Mulligan, R.P., Horton, B.P., 2017b. Extended late Holocene relative sea-level histories for North Carolina, USA. Quaternary Science Reviews 160, 13-30.

Kemp, A.C., Sommerfield, C.K., Vane, C.H., Horton, B.P., Chenery, S.R., Anisfeld, S.C., Nikitina, D., 2012a. Use of lead isotopes for developing chronologies in recent salt-marsh sediments. Quaternary Geochronology 12, 40-49.

Kemp, A.C., Telford, R.J., 2015. Transfer Functions, in: Shennan, I., Long, A.J., Horton, B.P. (Eds.), Handbook for Sea-Level Research. John Wiley & Sons, Chichester, pp. 470-499.

Kemp, A.C., Vane, C.H., Horton, B.P., Engelhart, S.E., Nikitina, D., 2012b. Application of stable carbon isotopes for reconstructing salt-marsh floral zones and relative sea level, New Jersey, USA. Journal of Quaternary Science 27, 404-414.

Kemp, A.C., Wright, A.J., Barnett, R.L., Hawkes, A.D., Charman, D.J., Sameshima, C., King, A.N., Mooney, H.C., Edwards, R.L., Horton, B.P., 2017c. Utility of salt-marsh foraminifera, testate amoebae and bulk-sediment $\delta^{13}C$ values as sea-level indicators in Newfoundland, Canada. Marine Micropaleontology 130.

Kenigson, J.S., Han, W., Rajagopalan, B., Yanto, Jasinski, M., 2018. Decadal shift of NAO-linked interannual sea level variability along the U.S. northeast coast. Journal of Climate 31, 4981-4989.

Kirwan, M.L., Guntenspergen, G.R., D'Alpaos, A., Morris, J.T., Mudd, S.M., Temmerman, S., 2010. Limits on the adaptability of coastal marshes to rising sea level. Geophysical Research Letters 37.

Kirwan, M.L., Temmerman, S., Skeehan, E.E., Guntenspergen, G.R., Fagherazzi, S., 2016. Overestimation of marsh vulnerability to sea level rise. Nature Climate Change 6, 253.

1259 Kopp, R.E., Horton, R.M., Little, C.M., Mitrovica, J.X., Oppenheimer, M., Rasmussen, D.J., Strauss, B.H., Tebaldi,
1260 C., 2014. Probabilistic 21st and 22nd century sea-level projections at a global network of tide-gauge sites. Earth's
1261 Future 2, 383-406.

1262 Kopp, R.E., Kemp, A.C., Bitterman, K., Horton, B.P., Donnelly, J.P., Gehrels, W.R., Hay, C., Mitrovica, J.X.,
1263 Morrow, E., Rahmstorf, S., 2016. Temperature-driven global sea-level variability in the Common Era. Proceedings
1264 of the National Academy of Sciences 113, E1434-E1441.

1265 Kuhlbrodt, T., Griesel, A., Montoya, M., Levermann, A., Hofmann, M., Rahmstorf, S., 2007. On the driving
1266 processes of the Atlantic meridional overturning circulation. Reviews of Geophysics 45, RG2001.

1267 Lambeck, K., Rouby, H., Purcell, A., Sun, Y., Sambridge, M., 2014. Sea level and global ice volumes from the Last
1268 Glacial Maximum to the Holocene. Proceedings of the National Academy of Sciences 111, 15296-15303.

1269 Lang, S., Brezger, A., 2004. Bayesian P-splines. Journal of Computational and Graphical Statistics 13, 183-212.

1270 Legendre, P., Birks, H.J.B., 2012. From Classical to Canonical Ordination, in: Birks, H.J.B., Lotter, A.F., Juggins,
1271 S., Smol, J.P. (Eds.), Tracking Environmental Change Using Lake Sediments: Data Handling and Numerical
1272 Techniques. Springer Netherlands, Dordrecht, pp. 201-248.

1273 Levermann, A., Griesel, A., Hofmann, M., Montoya, M., Rahmstorf, S., 2005. Dynamic sea level changes following
1274 changes in the thermohaline circulation. Clim Dyn 24, 347-354.

1275 Lima, A.L., Bergquist, B.A., Boyle, E.A., Reuer, M.K., Dudas, F.O., Reddy, C.M., Eglinton, T.I., 2005. High-
1276 resolution historical records from Pettaquamscutt River basin sediments: 2. Pb isotopes reveal a potential new
1277 stratigraphic marker. Geochimica et Cosmochimica Acta 69, 1813-1824.

1278 Long, A.J., Waller, M.P., Stupples, P., 2006. Driving mechanisms of coastal change: Peat compaction and the
1279 destruction of late Holocene coastal wetlands. Marine Geology 225, 63-84.

1280 Long, A.J., Woodroffe, S.A., Milne, G.A., Bryant, C.L., Simpson, M.J.R., Wake, L.M., 2012. Relative sea-level
1281 change in Greenland during the last 700yrs and ice sheet response to the Little Ice Age. Earth and Planetary Science
1282 Letters 315-316, 76-85.

1283 Love, R., Milne, G.A., Tarasov, L., Engelhart, S.E., Hijma, M., Latychev, K., Horton, B.P., Tornqvist, T., 2016.
1284 Projections of sea level change along the east and Gulf coasts of North America. Earth's Future 4, 440-464.

1285 Marcott, S.A., Shakun, J.D., Clark, P.U., Mix, A.C., 2013. A reconstruction of regional and global temperature for
1286 the past 11,300 years. Science 339, 1198-1201.

1287 Marsicek, J., Shuman, B.N., Bartlein, P.J., Shafer, S.L., Brewer, S., 2018. Reconciling divergent trends and
1288 millennial variations in Holocene temperatures. Nature 554, 92.

1289 McCarthy, G., Frajka-Williams, E., Johns, W.E., Baringer, M.O., Meinen, C.S., Bryden, H.L., Rayner, D., Duchez,
1290 A., Roberts, C., Cunningham, S.A., 2012. Observed interannual variability of the Atlantic meridional overturning
1291 circulation at 26.5°N. Geophysical Research Letters 39, L19609.

1292 McCarthy, G.D., Haigh, I.D., Hirschi, J.J.M., Grist, J.P., Smeed, D.A., 2015. Ocean impact on decadal Atlantic
1293 climate variability revealed by sea-level observations. Nature 521, 508-510.

1294 McHutchon, A., Rasmussen, C.E., 2011. Gaussian process training with input noise, Advances in Neural
1295 Information Processing Systems, pp. 1341-1349.

1296 Meade, R.H., Emery, K.O., 1971. Sea level as affected by river runoff, eastern United States. Science 173, 425-428.

Mitrovica, J.X., Gomez, N., Clark, P.U., 2009. The sea-level fingerprint of West Antarctic collapse. Science 323, 753.

Mitrovica, J.X., Gomez, N., Morrow, E., Hay, C., Latychev, K., Tamisiea, M.E., 2011. On the robustness of predictions of sea level fingerprints. Geophysical Journal International 187, 729-742.

Morris, J.T., Sundareshwar, P.V., Nietch, C.T., Kjerfve, B., Cahoon, D.R., 2002. Response of coastal wetlands to rising sea level. Ecology 83, 2869-2877.

Niering, W.A., Warren, R.S., Weymouth, C.G., 1977. Our dynamic tidal marshes: vegetation changes as revealed by peat analysis, The Connecticut Arboretum Bulletin, 22 ed, p. 12.

Ortega, P., Lehner, F., Swingedouw, D., Masson-Delmotte, V., Raible, C.C., Casado, M., Yiou, P., 2015. A model-tested North Atlantic Oscillation reconstruction for the past millennium. Nature 523, 71-74.

PAGES2k, C., 2017. A global multiproxy database for temperature reconstructions of the Common Era. Scientific Data 4, 170088.

Parnell, A.C., Haslett, J., Allen, J.R.M., Buck, C.E., Huntley, B., 2008. A flexible approach to assessing synchroneity of past events using Bayesian reconstructions of sedimentation history. Quaternary Science Reviews 27, 1872-1885.

Peltier, W.R., 1996. Global sea level rise and glacial isostatic adjustment: an analysis of data from the east coast of North America. Geophysical Research Letters 23, GL00848.

Peltier, W.R., 2004. Global glacial isostasy and the surface of the ice-age Earth: the ICE-5G (VM2) model and GRACE. Annual Review of Earth and Planetary Sciences 32, 111-149.

Peltier, W.R., Argus, D.F., Drummond, R., 2015. Space geodesy constrains ice-age terminal deglaciation: the ICE-6G_C (VM5a) model. Journal of Geophysical Research: Solid Earth 120, 450-487.

Piecuch, C.G., Dangendorf, S., Ponte, R.M., Marcos, M., 2016. Annual sea level changes on the North American northeast coast: influence of local winds and barotropic motions. Journal of Climate 29, 4801-4816.

Piecuch, C.G., Huybers, P., Hay, C., Kemp, A.C., Little, C.M., Mitrovica, J.X., Ponte, R.M., Tingley, M.P., Accepted. Origin of spatial variation in United States East Coast sea level trends during 1900–2016. Nature.

Rasmussen, C.E., Williams, C.I.K., 2005. Gaussian Processes for Machine Learning. Massachusetts Institue of Technology Press.

Redfield, A.C., 1972. Development of a New England salt marsh. Ecological Monographs 42, 201-237.

Rees, S., 2014. Adaptive oedometer automation, The Geotechnica, pp. 27-32.

Reimer, P.J., Bard, E., Bayliss, A., Beck, J.W., Blackwell, P.G., Bronk Ramsey, C., Grootes, P.M., Guilderson, T.P., Haflidason, H., Hajdas, I., Hatté, C., Heaton, T.J., Hoffmann, D.L., Hogg, A.G., Hughen, K.A., Kaiser, K.F., Kromer, B., Manning, S.W., Niu, M., Reimer, R.W., Richards, D.A., Scott, E.M., Southon, J.R., Staff, R.A., Turney, C.S.M., van der Plicht, J., 2013. IntCal13 and Marine13 radiocarbon age calibration curves 0–50,000 years cal BP. Radiocarbon 55, 1869-1887.

Richard, G.A., 1978. Seasonal and environmental variations in sediment accretion in a Long Island salt marsh. Estuaries 1, 29-35.

Roberts, B.A., Robertson, A., 1986. Salt marshes of Atlantic Canada: their ecology and distribution. Canadian Journal of Botany 64, 455-467.

Roemmich, D., Gilson, J., 2009. The 2004–2008 mean and annual cycle of temperature, salinity, and steric height in the global ocean from the Argo Program. Progress in Oceanography 82, 81-100.

Roy, K., Peltier, W.R., 2015. Glacial isostatic adjustment, relative sea level history and mantle viscosity: Reconciling relative sea level model predictions for the U.S. East coast with geological constraints. Geophysical Journal International 201, 1156-1181.

Sallenger, A.H., Doran, K.S., Howd, P.A., 2012. Hotspot of accelerated sea-level rise on the Atlantic coast of North America. Nature Climate Change 2, 884-888.

Scott, D.B., Medioli, F.S., 1978. Vertical zonations of marsh foraminifera as accurate indicators of former sea levels. Nature 272, 528-531.

Shennan, I., Horton, B., 2002. Holocene land- and sea-level changes in Great Britain. Journal of Quaternary Science 17, 511-526.

Simpson, G.L., 2012. Analogue methods, in: Birks, H.J.B., Lotter, A.F., Juggins, S., Smol, J.P. (Eds.), Data Handling and Numerical Techniques. Springer, Dordrecht, pp. 495-522.

Stockmarr, J., 1971. Tablets with spores used in absolute pollen analysis. Pollen et Spores 13, 615-621.

Stuiver, M., Polach, H.A., 1977. Reporting of ^{14}C data. Radiocarbon 19, 355-363.

Stuiver, M., Reimer, P.J., Reimer, R.W., 2017. Calib, 7.1 ed.

Team, R.C.D., 2017. R: A language and environment for statistical computing, 3.4.2 ed. R Foundation for Statistical Computing, Vienna, Austria.

Thomas, E., Varekamp, J., 1991. Paleo-environmental analysis of marsh sequences (Clinton, CT); evidence for punctuated sea-level rise during the latest Holocene. Journal of Coastal Research 11, 125-158.

Thornalley, D.J.R., Oppo, D.W., Ortega, P., Robson, J.I., Brierley, C.M., Davis, R., Hall, I.R., Moffa-Sanchez, P., Rose, N.L., Spooner, P.T., Yashayaev, I., Keigwin, L.D., 2018. Anomalously weak Labrador Sea convection and Atlantic overturning during the past 150 years. Nature 556, 227-230.

Trouet, V., Esper, J., Graham, N.E., Baker, A., Scourse, J.D., Frank, D.C., 2009. Persistent positive North Atlantic oscillation mode dominated the medieval climate anomaly. Science 324, 78-80.

Watcham, E.P., Shennan, I., Barlow, N.L.M., 2013. Scale considerations in using diatoms as indicators of sea-level change: lessons from Alaska. Journal of Quaternary Science 28, 165-179.

Weidick, A., Kelly, M., Bennike, O., 2004. Late Quaternary development of the southern sector of the Greenland Ice Sheet, with particular reference to the Qassimiut lobe. Boreas 33, 284-299.

Willis, J.K., Roemmich, D., Cornuelle, B., 2004. Interannual variability in upper ocean heat content, temperature, and thermosteric expansion on global scales. Journal of Geophysical Research: Oceans 109.

Wilson, C.A., Hughes, Z.J., FitzGerald, D.M., Hopkinson, C.S., Valentine, V., Kolker, A.S., 2014. Saltmarsh pool and tidal creek morphodynamics: Dynamic equilibrium of northern latitude saltmarshes? Geomorphology 213, 99-115.

Wilson, K.R., Kelley, J.T., Tanner, B.R., Belknap, D.F., 2010. Probing the origins and stratigraphic signature of salt pools from north-temperate marshes in Maine, USA. Journal of Coastal Research 26, 1007-1026.

Woodworth, P.L., Morales Maqueda, M.Á., Gehrels, W.R., Roussenov, V.M., Williams, R.G., Hughes, C.W., 2017. Variations in the difference between mean sea level measured either side of Cape Hatteras and their relation to the North Atlantic Oscillation. Clim Dyn 49, 2451-2469.

Wright, A.J., Edwards, R.J., van de Plassche, O., 2011. Reassessing transfer-function performance in sea-level reconstruction based on benthic salt-marsh foraminifera from the Atlantic coast of NE North America. Marine Micropaleontology 81, 43-62.

Wright, A.J., van de Plassche, O., 2001. Field Guide to the Quaternary west coast of Newfoundland. Geological Association of Canada - Mineralogical Association of Canada.

Wright, S.M., Howard, B.J., Strand, P., Nylén, T., Sickel, M.A.K., 1999. Prediction of ^{137}Cs deposition from atmospheric nuclear weapons tests within the Arctic. Environmental Pollution 104, 131-143.

Zoccarato, C., Teatini, P., 2017. Numerical simulations of Holocene salt-marsh dynamics under the hypothesis of large soil deformations. Advances in Water Resources 110, 107-119.

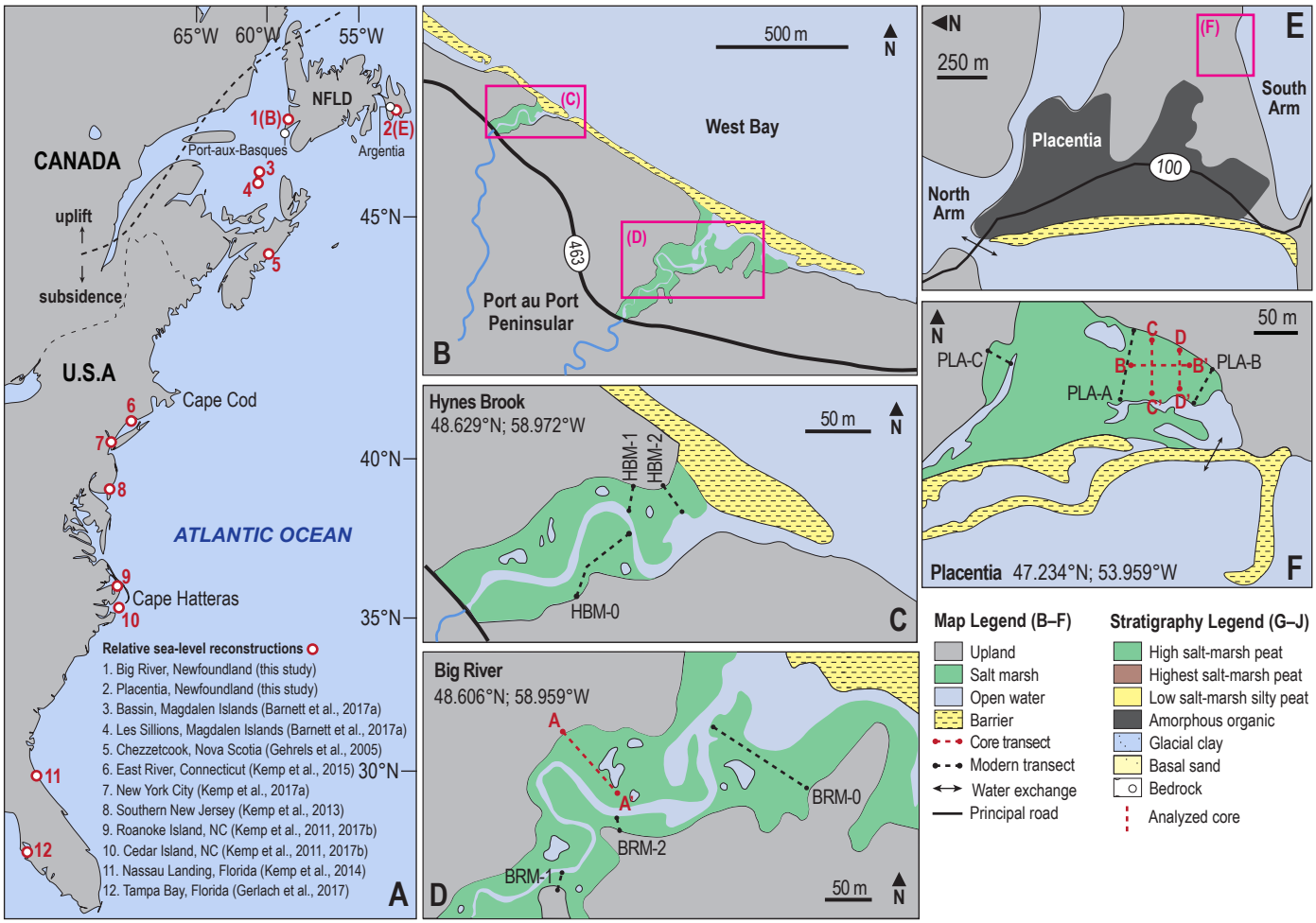
65°W
60°W
55°W
NFLD
CANADA
Port-aux-Basques
Argentia
1(B)
2(E)
3
4
5
uplift
subsidence
45°N
U.S.A
Cape Cod
6
7
8
40°N
ATLANTIC OCEAN
9
Cape Hatteras
10
35°N
11
12
30°N
Relative sea-level reconstructions
1. Big River, Newfoundland (this study)
2. Placentia, Newfoundland (this study)
3. Bassin, Magdalen Islands (Barnett et al., 2017a)
4. Les Sillions, Magdalen Islands (Barnett et al., 2017a)
5. Chezzetcook, Nova Scotia (Gehrels et al., 2005)
6. East River, Connecticut (Kemp et al., 2015)
7. New York City (Kemp et al., 2017a)
8. Southern New Jersey (Kemp et al., 2013)
9. Roanoke Island, NC (Kemp et al., 2011, 2017b)
10. Cedar Island, NC (Kemp et al., 2011, 2017b)
11. Nassau Landing, Florida (Kemp et al., 2014)
12. Tampa Bay, Florida (Gerlach et al., 2017)
A
500 m
N
(C)
West Bay
(D)
463
Port au Port
Peninsular
B
Hynes Brook
48.629°N; 58.972°W
50 m
N
HBM-1
HBM-2
HBM-0
C
Big River
48.606°N; 58.959°W
A
A'
BRM-0
BRM-2
BRM-1
50 m
N
D
N
250 m
(F)
E
South
Arm
Placentia
100
North
Arm
N
50 m
C
D
B
B'
PLA-C
PLA-B
PLA-A
C'
D'
Placentia 47.234°N; 53.959°W
F
Map Legend (B–F)
Upland
Salt marsh
Open water
Barrier
Core transect
Modern transect
Water exchange
Principal road
Stratigraphy Legend (G–J)
High salt-marsh peat
Highest salt-marsh peat
Low salt-marsh silty peat
Amorphous organic
Glacial clay
Basal sand
Bedrock
Analyzed core

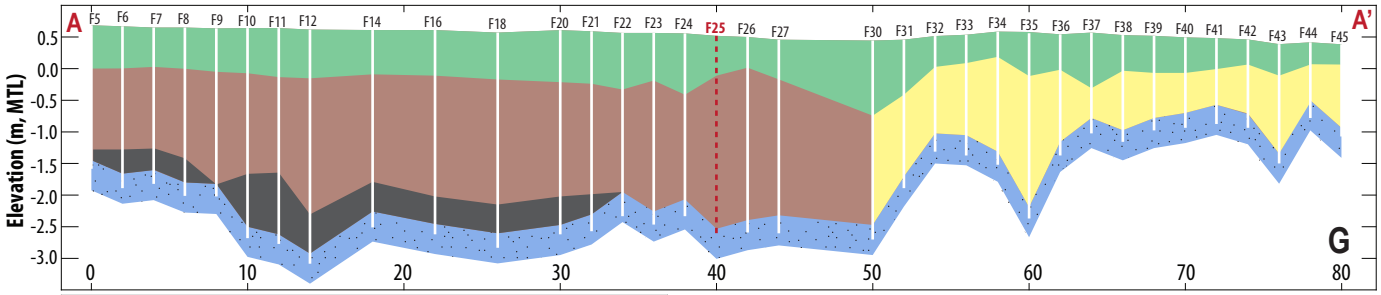
A
F5 F6 F7 F8 F9 F10 F11 F12 F14 F16 F18 F20 F21 F22 F23 F24 F25 F26 F27 F30 F31 F32 F33 F34 F35 F36 F37 F38 F39 F40 F41 F42 F43 F44 F45
A'
Elevation (m, MTL)
0.5
0.0
-0.5
-1.0
-1.5
-2.0
-2.5
-3.0
0
10
20
30
40
50
60
70
80
G

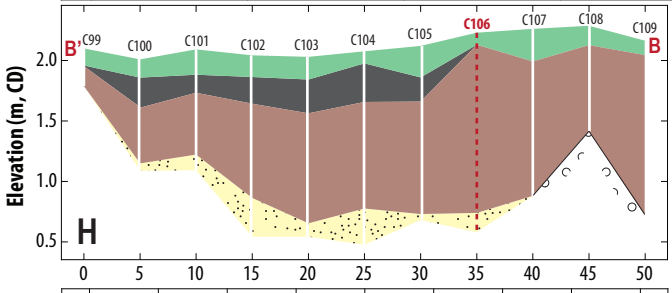
B'
C99 C100 C101 C102 C103 C104 C105 C106 C107 C108 C109
B
Elevation (m, CD)
2.0
1.5
1.0
0.5
0
5
10
15
20
25
30
35
40
45
50
H

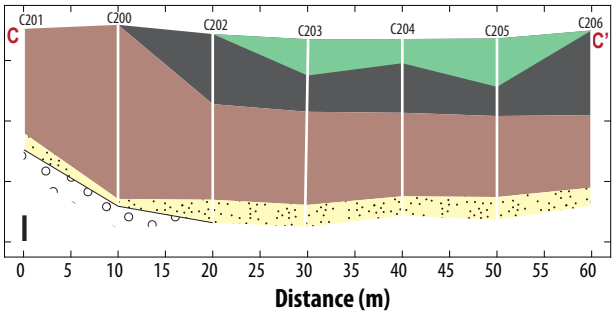
C
C201 C200 C202 C203 C204 C205 C206
C'
0
5
10
15
20
25
30
35
40
45
50
55
60
Distance (m)
I

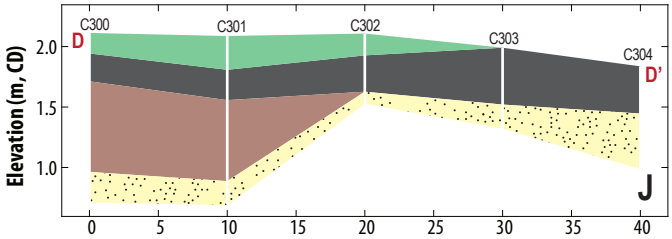
D
C300 C301 C302 C303 C304
D'
Elevation (m, CD)
2.0
1.5
1.0
0
5
10
15
20
25
30
35
40
J

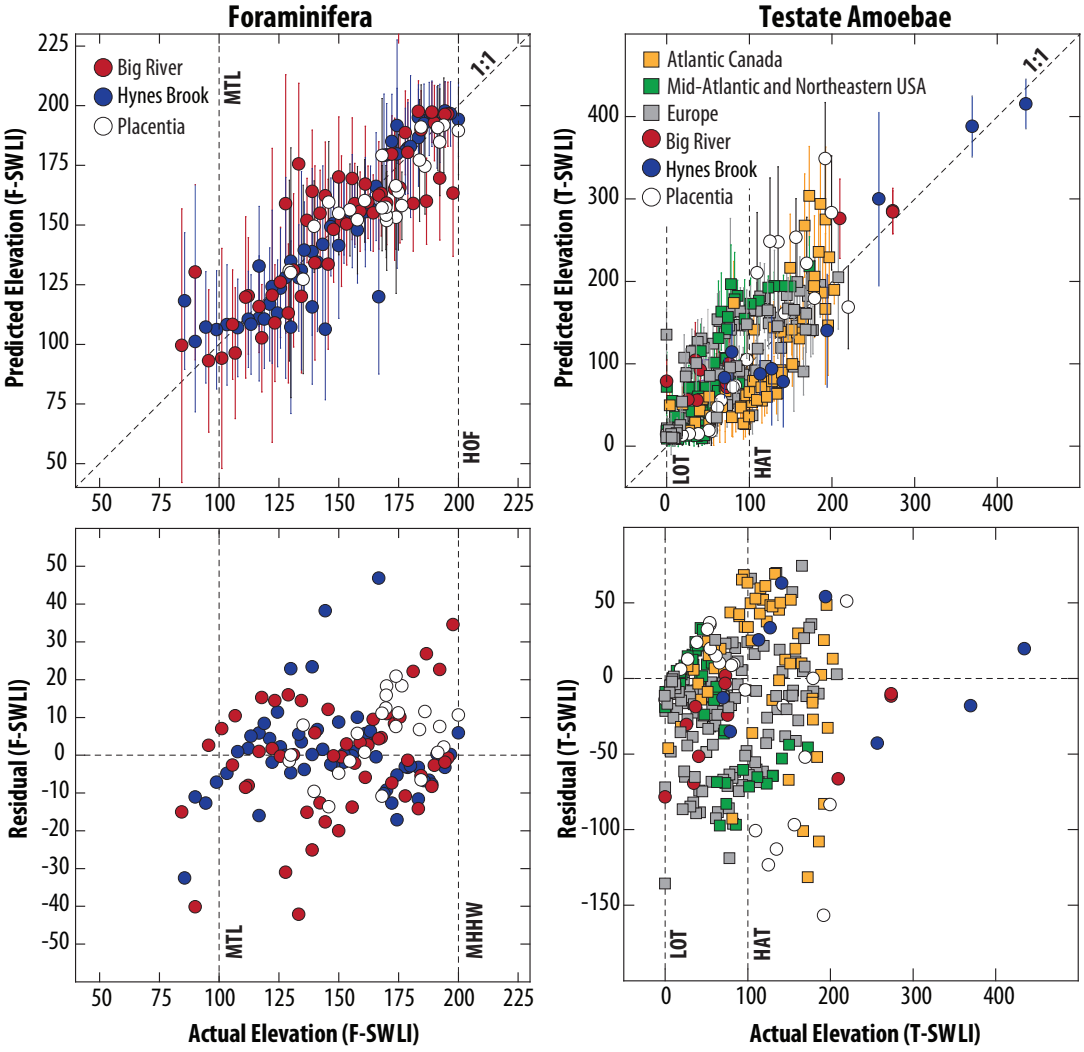
Foraminifera
Testate Amoebae
Big River
Hynes Brook
Placentia
Atlantic Canada
Mid-Atlantic and Northeastern USA
Europe
MTL
HOF
LOT
HAT
MHHW
1:1
Predicted Elevation (F-SWLI)
Predicted Elevation (T-SWLI)
Residual (F-SWLI)
Residual (T-SWLI)
Actual Elevation (F-SWLI)
Actual Elevation (T-SWLI)

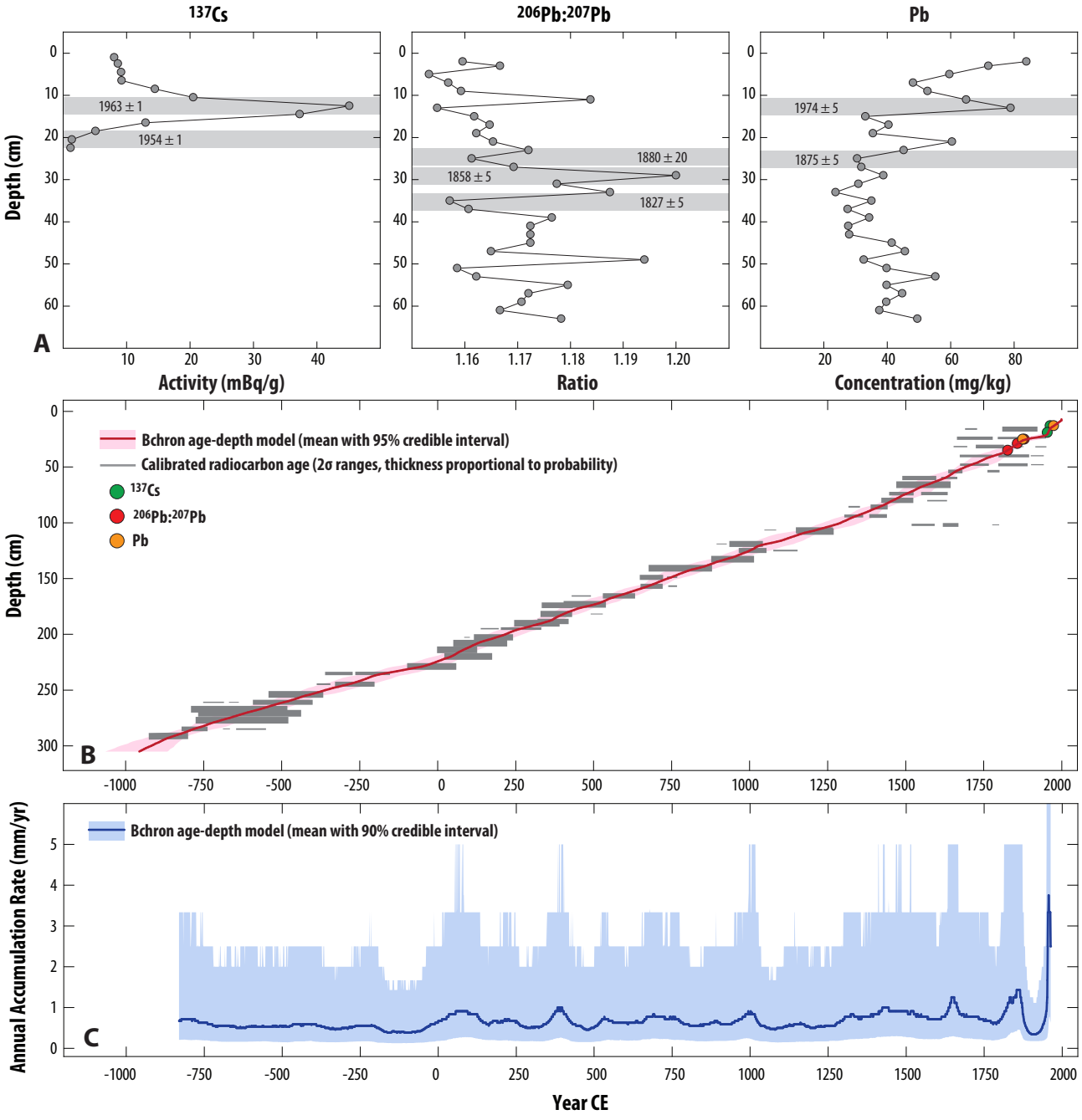
137Cs
206Pb:207Pb
Pb
Depth (cm)
1963 ± 1
1954 ± 1
1880 ± 20
1858 ± 5
1827 ± 5
1974 ± 5
1875 ± 5
A
Activity (mBq/g)
Ratio
Concentration (mg/kg)
Bchron age-depth model (mean with 95% credible interval)
Calibrated radiocarbon age (2σ ranges, thickness proportional to probability)
137Cs
206Pb:207Pb
Pb
B
Bchron age-depth model (mean with 90% credible interval)
Annual Accumulation Rate (mm/yr)
C
Year CE

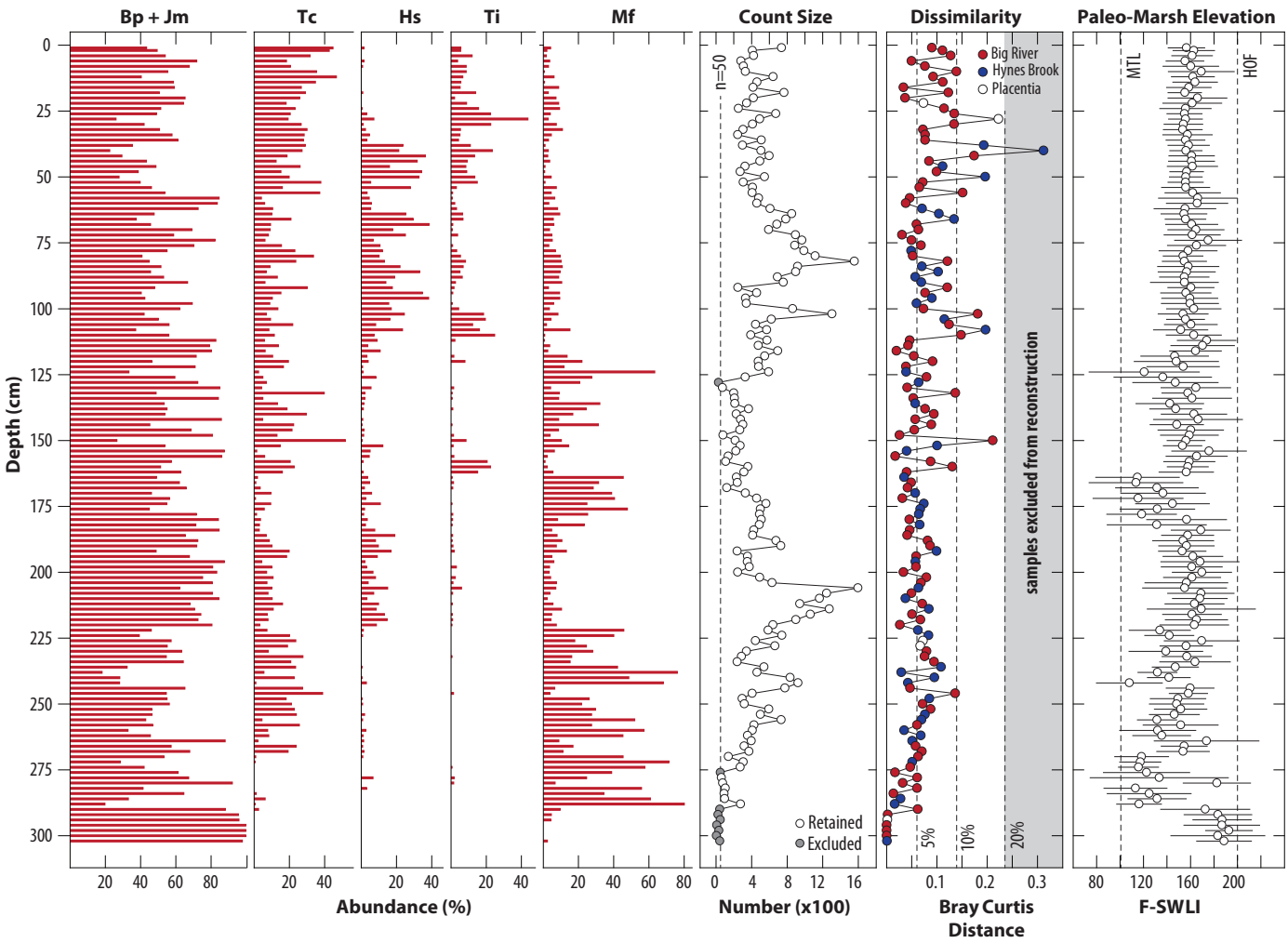
Bp + Jm
Tc
Hs
Ti
Mf
Count Size
Dissimilarity
Paleo-Marsh Elevation
Depth (cm)
0
25
50
75
100
125
150
175
200
225
250
275
300
20 40 60 80
20 40
20 40
20 40
20 40 60 80
Abundance (%)
n=50
Retained
Excluded
0 4 8 12 16
Number (x100)
Big River
Hynes Brook
Placentia
samples excluded from reconstruction
5%
10%
20%
0.1 0.2 0.3
Bray Curtis Distance
MTL
HOF
80 120 160 200
F-SWLI

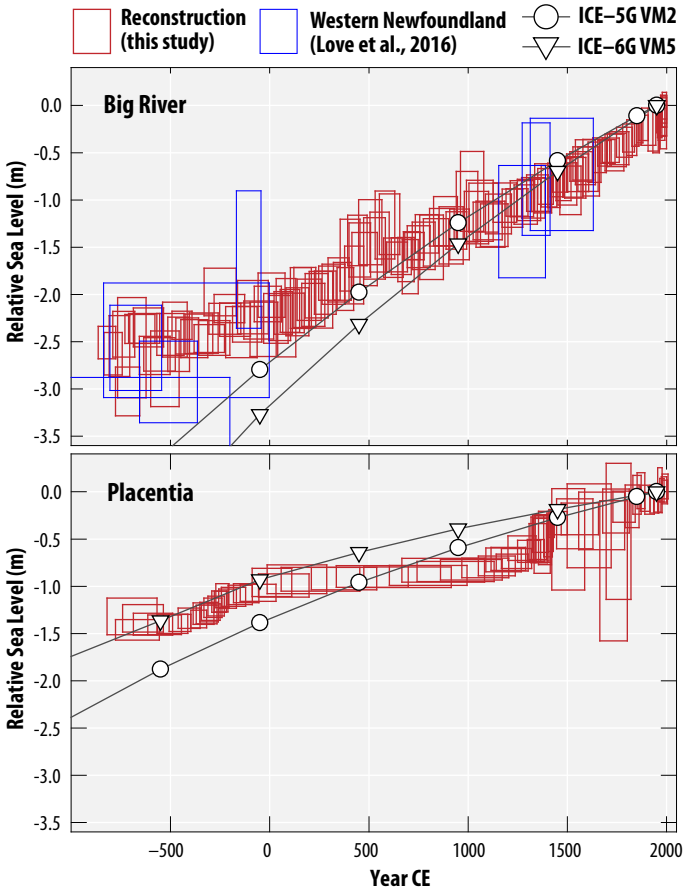
Reconstruction
(this study)
Western Newfoundland
(Love et al., 2016)
ICE–5G VM2
ICE–6G VM5
Big River
Placentia
Relative Sea Level (m)
0.0
-0.5
-1.0
-1.5
-2.0
-2.5
-3.0
-3.5
–500
0
500
1000
1500
2000
Year CE

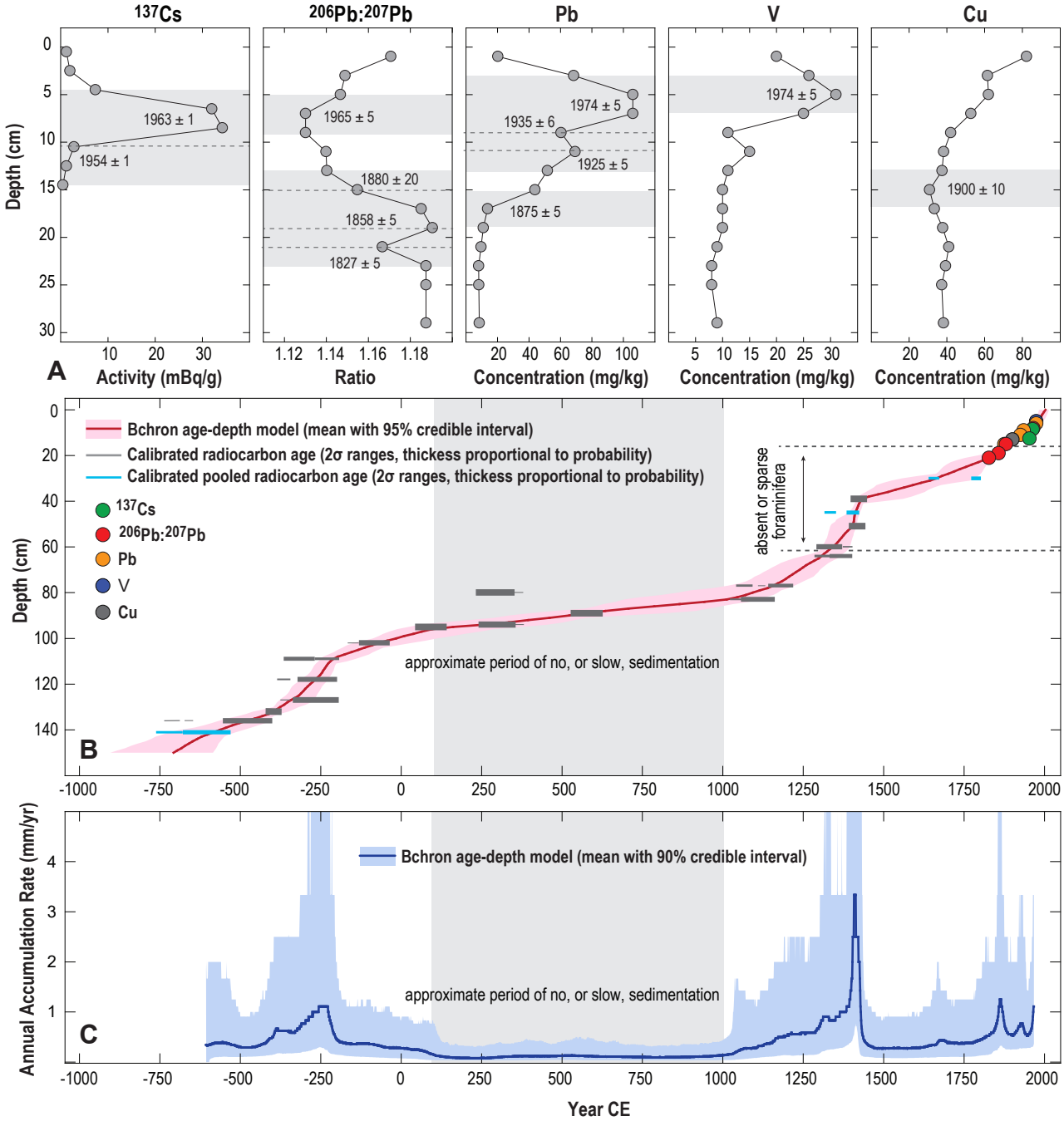
137Cs
206Pb:207Pb
Pb
V
Cu
Depth (cm)
1963 ± 1
1954 ± 1
1965 ± 5
1880 ± 20
1858 ± 5
1827 ± 5
1974 ± 5
1935 ± 6
1925 ± 5
1875 ± 5
1974 ± 5
1900 ± 10
Activity (mBq/g)
Ratio
Concentration (mg/kg)
Concentration (mg/kg)
Concentration (mg/kg)
A
Bchron age-depth model (mean with 95% credible interval)
Calibrated radiocarbon age (2σ ranges, thickess proportional to probability)
Calibrated pooled radiocarbon age (2σ ranges, thickess proportional to probability)
137Cs
206Pb:207Pb
Pb
V
Cu
absent or sparse foraminifera
approximate period of no, or slow, sedimentation
B
Annual Accumulation Rate (mm/yr)
Bchron age-depth model (mean with 90% credible interval)
approximate period of no, or slow, sedimentation
C
Year CE

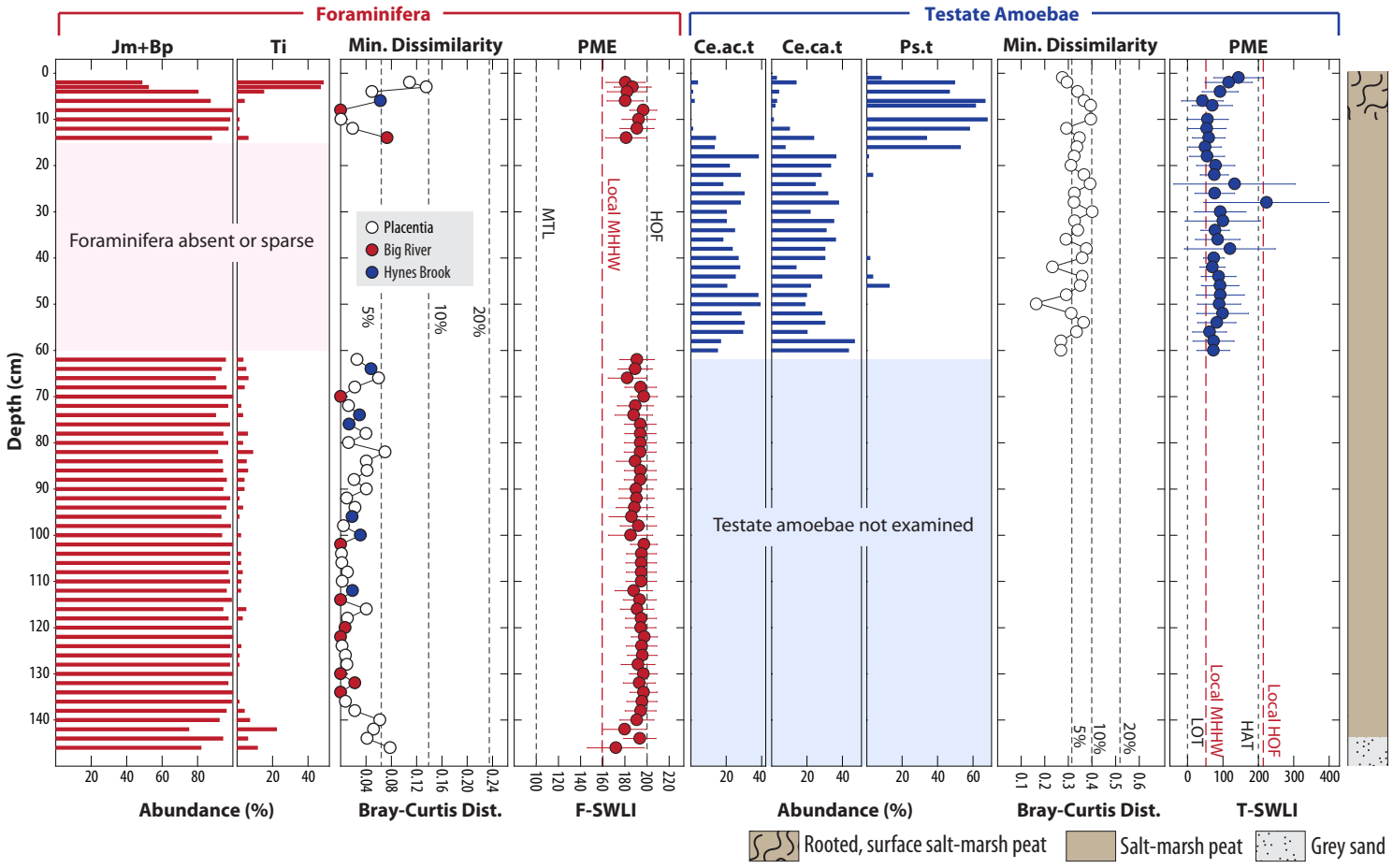
Foraminifera
Testate Amoebae
Jm+Bp
Ti
Min. Dissimilarity
PME
Ce.ac.t
Ce.ca.t
Ps.t
Min. Dissimilarity
PME
Depth (cm)
Foraminifera absent or sparse
Placentia
Big River
Hynes Brook
5%
10%
20%
MTL
Local MHHW
HOF
Testate amoebae not examined
5%
10%
20%
LOT
Local MHHW
HAT
Local HOF
Abundance (%)
Bray-Curtis Dist.
F-SWLI
Abundance (%)
Bray-Curtis Dist.
T-SWLI
Rooted, surface salt-marsh peat
Salt-marsh peat
Grey sand

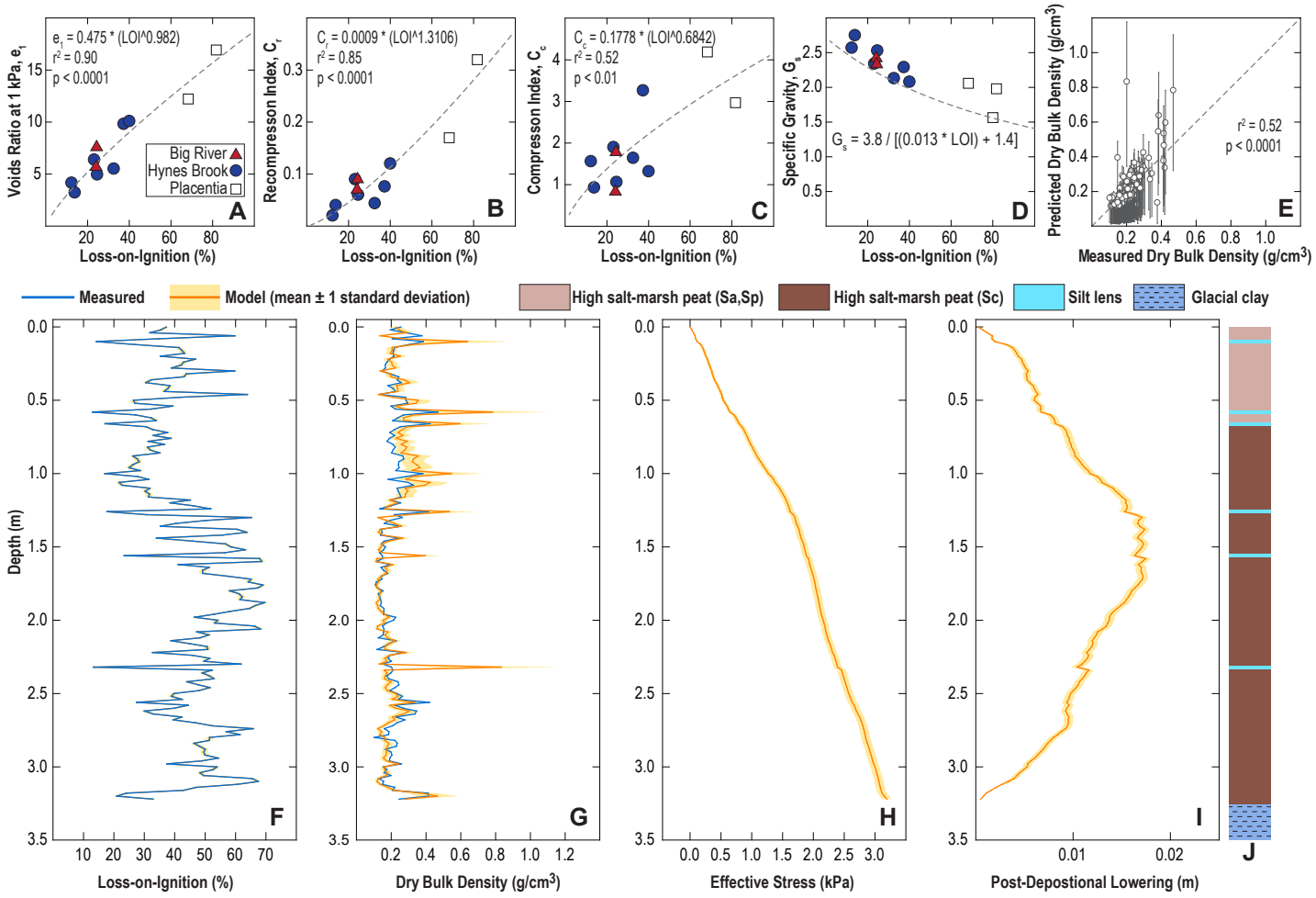
e1 = 0.475 * (LOI^0.982)
r2 = 0.90
p < 0.0001
Big River
Hynes Brook
Placentia
Voids Ratio at 1 kPa, e1
Loss-on-Ignition (%)
A
Cr = 0.0009 * (LOI^1.3106)
r2 = 0.85
p < 0.0001
Recompresson Index, Cr
B
Cc = 0.1778 * (LOI^0.6842)
r2 = 0.52
p < 0.01
Compresson Index, Cc
C
Gs = 3.8 / [(0.013 * LOI) + 1.4]
Specific Gravity, Gs
D
r2 = 0.52
p < 0.0001
Predicted Dry Bulk Density (g/cm3)
Measured Dry Bulk Density (g/cm3)
E
Measured
Model (mean ± 1 standard deviation)
High salt-marsh peat (Sa,Sp)
High salt-marsh peat (Sc)
Silt lens
Glacial clay
Depth (m)
Loss-on-Ignition (%)
F
Dry Bulk Density (g/cm3)
G
Effective Stress (kPa)
H
Post-Depostional Lowering (m)
I
J

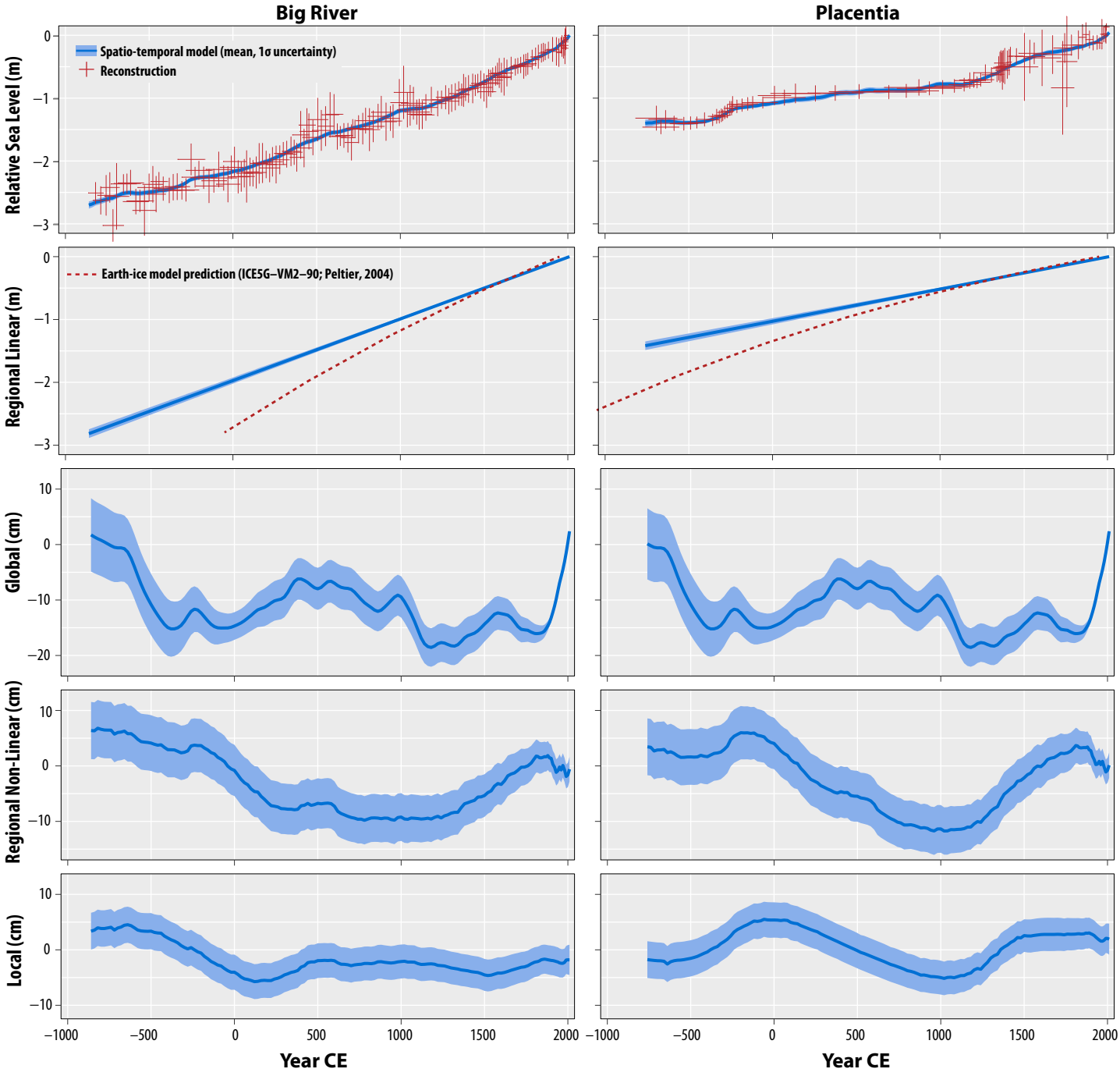
Big River
Placentia
Spatio-temporal model (mean, 1σ uncertainty)
Reconstruction
Earth-ice model prediction (ICE5G–VM2–90; Peltier, 2004)
Relative Sea Level (m)
Regional Linear (m)
Global (cm)
Regional Non-Linear (cm)
Local (cm)
0
−1
−2
−3
10
−10
−20
−1000
−500
0
500
1000
1500
2000
Year CE

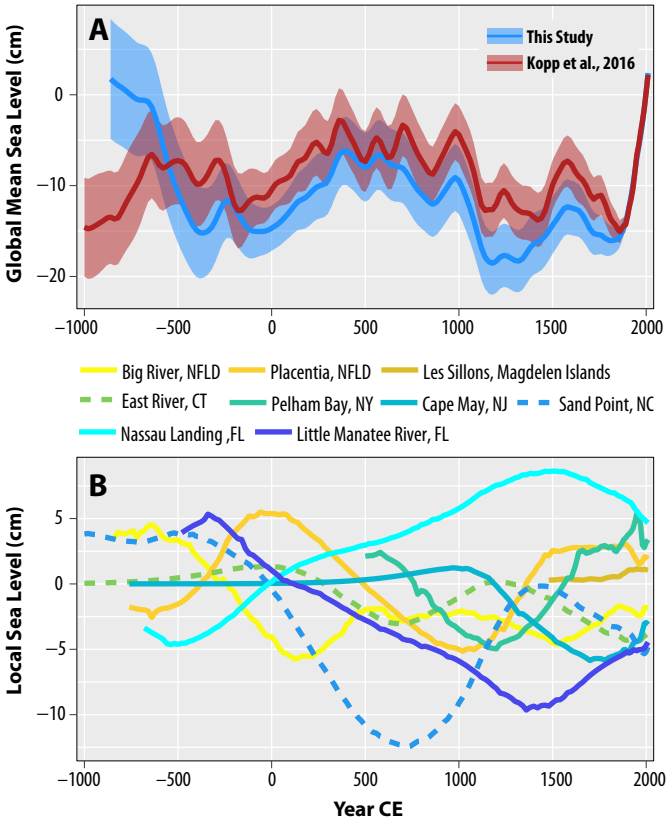
A
This Study
Kopp et al., 2016
Global Mean Sea Level (cm)
0
−10
−20
−1000
−500
0
500
1000
1500
2000
Big River, NFLD
Placentia, NFLD
Les Sillons, Magdelen Islands
East River, CT
Pelham Bay, NY
Cape May, NJ
Sand Point, NC
Nassau Landing ,FL
Little Manatee River, FL
B
Local Sea Level (cm)
5
0
−5
−10
−1000
−500
0
500
1000
1500
2000
Year CE

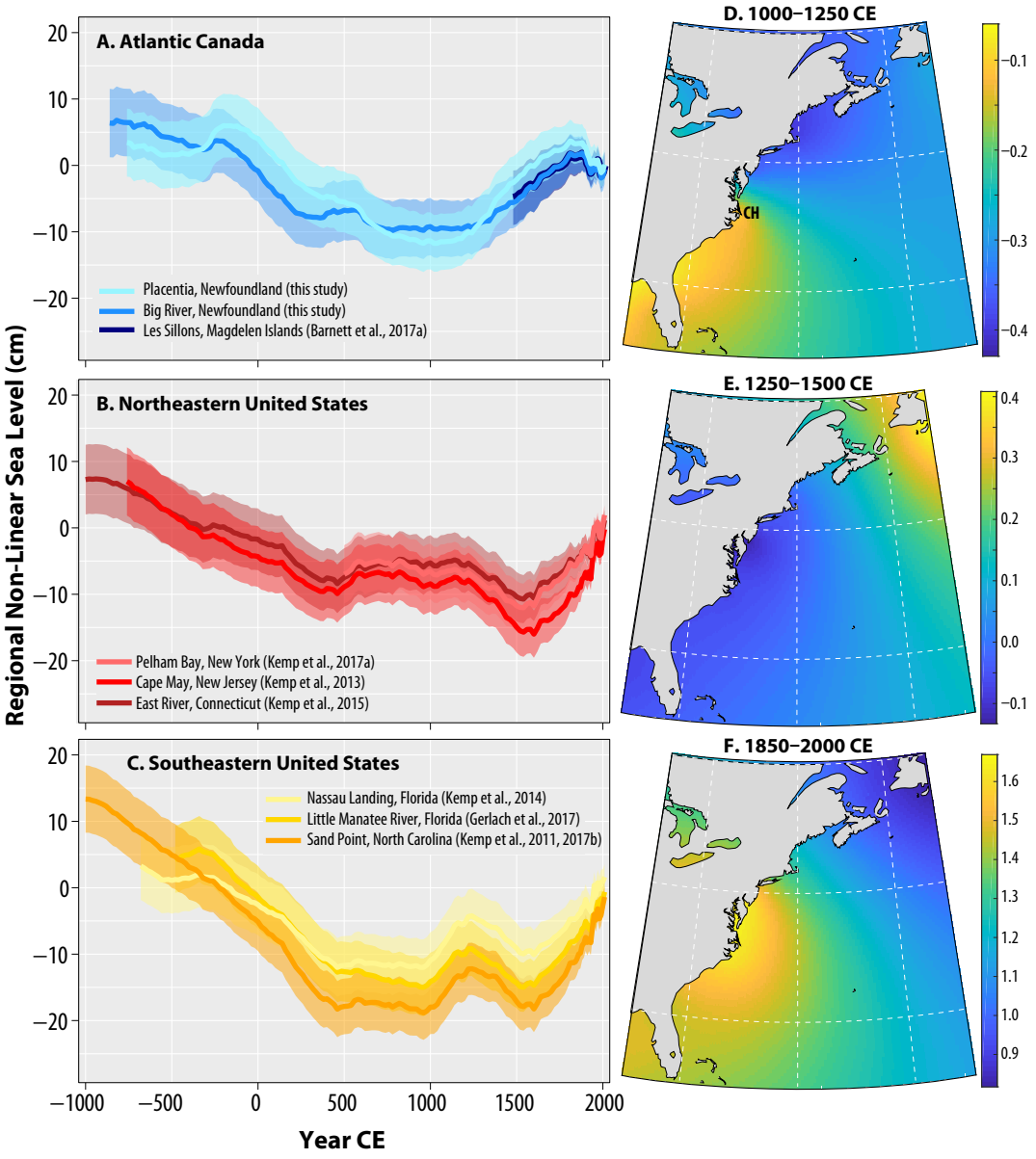
A. Atlantic Canada
Placentia, Newfoundland (this study)
Big River, Newfoundland (this study)
Les Sillons, Magdelen Islands (Barnett et al., 2017a)
B. Northeastern United States
Pelham Bay, New York (Kemp et al., 2017a)
Cape May, New Jersey (Kemp et al., 2013)
East River, Connecticut (Kemp et al., 2015)
C. Southeastern United States
Nassau Landing, Florida (Kemp et al., 2014)
Little Manatee River, Florida (Gerlach et al., 2017)
Sand Point, North Carolina (Kemp et al., 2011, 2017b)
Regional Non-Linear Sea Level (cm)
Year CE
D. 1000–1250 CE
E. 1250–1500 CE
F. 1850–2000 CE
CH